

Bubble-Turbulence Dynamics and Dissipation Beneath Laboratory Breaking Waves

ANDREW W. SMITH,^a BRIAN K. HAUS,^a AND RACHEL H. R. STANLEY^b

^a Rosenstiel School of Marine and Atmospheric Science, University of Miami, Miami, Florida
^b Wellesley College, Wellesley, Massachusetts

(Manuscript received 20 September 2021, in final form 21 May 2022)

ABSTRACT: Bubbles directly link sea surface structure to the dissipation rate of turbulence in the ocean surface layer through wave breaking, and they are an important vehicle for air-sea transfer of heat and gases and important for understanding both hurricanes and global climate. Adequate parameterization of bubble dynamics, especially in high winds, requires simultaneous measurements of surface waves and breaking-induced turbulence; collection of such data would be hazardous in the field, and they are largely absent from laboratory studies to date. We therefore present data from a series of laboratory wind-wave tank experiments designed to observe bubble size distributions in natural seawater beneath hurricane conditions and connect them to surface wave statistics and subsurface turbulence. A shadowgraph imager was used to observe bubbles in three different water temperature conditions. We used these controlled conditions to examine the role of stability, surface tension, and water temperature on bubble distributions. Turbulent kinetic energy dissipation rates were determined from subsurface ADCP data using a robust inertial-subrange identification algorithm and related to wind input via wave-dependent scaling. Bubble distributions shift from narrow to broadband and toward smaller radius with increased wind input and wave steepness. TKE dissipation rate and shear were shown to increase with wave steepness; this behavior is associated with a larger number of small bubbles in the distributions, suggesting shear is dominant in forcing bubbles in hurricane wind-wave conditions. These results have important implications for bubble-facilitated air-sea exchanges, near-surface ocean mixing, and the distribution of turbulence beneath the air-sea interface in hurricanes.

SIGNIFICANCE STATEMENT: Bubbles are a vehicle for the flux of heat, momentum, and gases between the atmosphere and ocean. These fluxes contribute to the energy budgets of hurricanes, climate, and upper-ocean biology. Few to no simultaneous measurements of surface waves, bubbles, and turbulence have been made in hurricane conditions. To improve numerical model representation of bubbles, we performed laboratory experiments to parameterize bubble size distributions using physical variables including wind and waves. Bubble distributions were found to become broadband and shift toward smaller radius with increased wind stress and wave steepness. Turbulence dissipation rate and shear were shown to increase with wave steepness. Our results give the first physically based bubble distribution parameterization from naturally breaking waves in hurricane-force conditions.

KEYWORDS: Atmosphere; Ocean; Turbulence; Wave breaking; Wave properties; Oceanic waves; Air-sea interaction; Chemistry, oceanic; Fluxes; Optical properties

1. Introduction

Bubbles are a captivating visual cue of processes intrinsic to the evolving sea surface and an important participant in air-sea exchanges. A complete understanding of bubble dynamics remains elusive but is imperative to quantifying gas transfer and improving climate and hurricane numerical models (Stanley et al. 2009; Brumer et al. 2017). Intermittent destabilization of the sea surface results in wave breaking events that entrain air and generate turbulence. This turbulence fragments the volume of air into groups or plumes of bubbles (Holthuijsen and Herbers 1986; Gemmrich 2010). Subsequently, these bubbles alter subsurface optical properties, scatter sound, contribute to marine aerosol production, and enhance air-sea gas flux; their diverse role in air-sea interaction and ocean surface layer dynamics has been investigated in field and laboratory studies for decades (e.g., Blanchard and

Woodcock 1957; Medwin 1970; Johnson and Cooke 1979; Deane and Stokes 1999). Since the earliest studies, size distribution has been observed to be the most important quantifiable property of a bubble population (Deane and Stokes 2002).

The initial size distribution of a bubble population and its subsequent evolution are the direct result of turbulence induced by the entraining event (i.e., wave breaking), ambient water environment, and the physical forces acting to maintain, grow, or disrupt the structure of the bubbles. Surface tension and breaking-induced turbulence act as opposing forces in determining the longevity of bubbles and their size evolution. Time-varying pressure fluctuations from the sea surface displacement and deforming stresses from shear-induced turbulence both contribute, aiding to shrink, grow, or fragment the bubbles. Within actively breaking wave crests, Hinze's formula (cf. Hinze 1955) quantifies the scale or maximum size a bubble can attain and resist fragmentation by turbulence,

Corresponding author: Andrew W. Smith, andrew.smith@rsmas.miami.edu

$$a_H = (D_{\max}/2) = 2^{-8/5} \varepsilon^{-2/5} \left(\frac{\sigma W e_c}{\rho} \right)^{3/5}, \quad (1)$$

where a_H is the Hinze scale (equal to half the maximum expected bubble diameter D_{\max}), ε is the turbulent kinetic energy (TKE) dissipation rate, σ is the surface tension, and $We_c = (\rho_w 2\varepsilon^{2/3} D_{\max}^{5/3} / \sigma)$ is the critical Weber number at which the bubble fragments; We_c has been experimentally found to lie in the range 3–4.7 (Deane and Stokes 2002). Through Eq. (1), the size distribution of bubbles observed beneath the air-sea interface is directly connected to turbulence, water density (i.e., temperature, salinity), and surface tension. Therefore, it is clear that adequate parameterization of bubble size distributions requires simultaneous measurements of the surface wave field and the bubble populations themselves, and that the dissipation of surface wave energies via breaking surface is critically linked to both bubble plume composition as well as measured subsurface turbulence.

Wave growth, evolution, and breaking have been observed in the field and investigated in the laboratory (e.g., Thorpe and Stubbs 1979; Koga 1982; Rapp and Melville 1990; Drennan et al. 1996), but with critically limiting caveats. Field studies, such as those conducted in the surf zone or from research vessels and platforms (Deane 1997; Holthuijsen and Herbers 1986; Gemmrich and Farmer 2004), are site-specific and constrained by the stochastic nature of wave breaking. The lack of predictability and control in these open-ocean settings has placed limitations on data quality and replication compared to what is achievable in the laboratory. Conversely, the bubble populations analyzed in most prior laboratory experiments have been produced by waves breaking in an unrealistic manner. Popular mechanisms in the literature for this unnatural bubble entrainment have included dispersive focusing of waves, tipping buckets, and forced injection by jets, pipettes, or pumps through fixed-diameter orifices (Rapp and Melville 1990; Hwang et al. 1991; Rensen et al. 2005) without wind forcing. Additionally, even where natural wave breaking has been observed in the open ocean, it has served as background context for observed bubble populations rather than being directly linked via statistics to the size and number of bubbles actually seen.

Given the limitations in earlier studies, particularly including an outstanding deficit of direct bubble and air-sea gas exchange measurements in hurricanes, we conducted a series of novel laboratory wind-wave tank experiments that provide the first simultaneous measurements of wind-forced wave-breaking-induced bubble populations and subsurface turbulence measured in natural seawater up to hurricane force conditions. Bubble size distributions observed are directly linked to evolution of the sea surface wave field, changes in ambient water properties, and wave-scaled subsurface turbulence (Hwang et al. 1991; Drennan et al. 1996; Terray et al. 1996).

2. Data

a. Experiments

The experiments were conducted in the Surge-Structure-Atmosphere Interaction facility wind-wave tank (hereafter SUSTAIN) at the University of Miami's Rosenstiel School of

Marine and Atmospheric Sciences (RSMAS) from 10 to 14 July 2018. SUSTAIN is 23 m long \times 6 m wide \times 2 m high with an 18-m test section composed of acrylic wall panels to facilitate optical measurements and flow visualization. The acrylic tank is mounted within a stainless steel frame and concrete, permitting rigid instrumentation installations within and through ceiling panels at specific fetches. Wind is driven by a 1460-horsepower fan and forced through a flow collimator honeycomb array into the test section via a gently sloping adjustable flap to avoid jump discontinuities as the wind meets the water surface.

Twelve independently operating HR Wallingford mechanical piston-action wave paddles are situated directly below the wind inlet and are controlled through computer software linkages and a user interface. When in use together, SUSTAIN is capable of producing 10-m equivalent wind speeds in excess of 100 m s^{-1} (223.7 mph) and single-amplitude (monochromatic), spectral, and dispersive-focused waves with modified along-crest structure or spreading. Additionally, the SUSTAIN facility is equipped with a boiler-fed through-flow pump and heat exchanger that allows for specific set-point water temperatures to be achieved in the tank water volume; this capability was particularly crucial to the experimental design. A schematic of SUSTAIN with instrument locations indicated with symbols is shown in Fig. 1.

Thirty-five independent experiments comprised this study, each with a specific water temperature, wind speed, and wave condition. Wind speeds spanned the range $10.6\text{--}50 \text{ m s}^{-1}$ and either monochromatic or JONSWAP (Joint North Sea Waves Project) spectral (e.g., Hasselmann et al. 1973) waves were produced. Since one of the primary goals of this collaborative study was to quantify bubble gas transfer and dynamics, the length of each experiment was governed by the noble gas mole ratios and saturation state, which were monitored throughout each experiment. A gas equilibration period with weak wind and gentle waves was necessary between each experiment. Water temperature set points for the experiments were 20° , 26° , and 32°C and were monitored at two depths and four locations within the tank. Noble gases included neon (Ne), argon (Ar), krypton (Kr), xenon (Xe), helium (He), and oxygen gas (O_2), and were measured in undersaturated and supersaturated conditions in different subsets of experiments. The gas saturation conditions were as listed prior to the experiment(s) indicated. A full summary of the experimental conditions is given in Table 1.

b. Instrumentation

1) AIR SIDE AND AT INTERFACE

Instruments were positioned near the middle of the SUSTAIN tank due to ease of access and to allow for wave development (see Fig. 1). Noble gas measurements and discrete gas concentration samples were taken from the midtank region of the testing section ($\approx 9.10\text{--}10.6\text{-m fetch}$) using a gas equilibrator mass spectrometer (GEMS; Manning et al. 2016), copper tube samples that were brought to the Woods Hole Oceanographic Institution (WHOI) Isotope

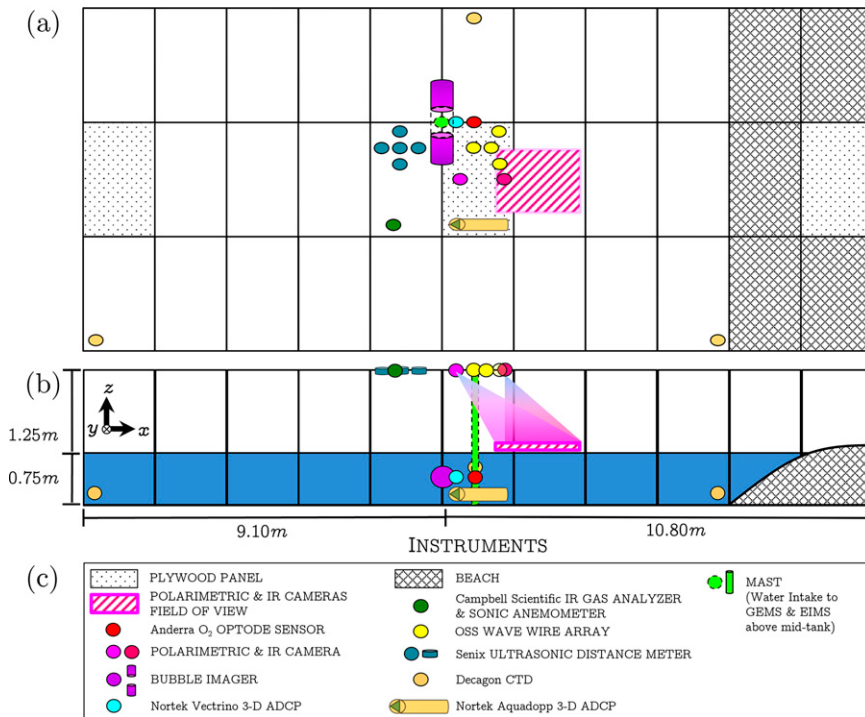


FIG. 1. Schematic of the test section of the SUSTAIN facility wind-wave tank. Wind/airflow was blown in the direction of the positive x axis. The instrument locations are indicated with symbols. (a) Above-tank view, showing the position of instruments. The bubble imager has two separate cylindrical nodes, which are depicted in purple here at about 9-m fetch. (b) Side view of the tank, with instrument locations shown. Note that the instruments have different cross-tank positions along the positive y axis. (c) Schematic symbols legend. Schematic not to scale.

Geochemistry Facility for analysis, equilibrator inlet mass spectrometer (EIMS; Cassar et al. 2009), and an optode oxygen gas sensor. The GEMS and EIMS units were mounted on a crane-suspended platform above the SUSTAIN mid-tank panel to minimize momentum transfer and vibrations. GEMS and EIMS provided continuous noble gas mole ratios (Ne/Xe , Kr/Xe , etc.) and O_2/Ar mole ratios, respectively; the two mass spectrometers were continuously

routed subsurface water from SUSTAIN via a water pump relay system. Discrete noble gas samples for measuring actual concentrations were taken using copper tube sampling on water transported by the same submersible water pump. The specific details of the noble gas measurement strategy and instrumentation are outside the scope of this manuscript; however, we direct interested readers to Kinjo (2019).

TABLE 1. Experimental conditions in SUSTAIN. The column headers refer to experiment number, water temperature (T_w), wave type either monochromatic or JONSWAP spectrum, dominant wave frequency (f) or peak period (T_p), amplitude (a) or significant wave height (H_s), and gas saturation conditions in the water.

Expt No.	T_w (°C)	U_{10} (m s ⁻¹)	Wave type ^a	f (Hz) or T_p (s)	a (m) or H_s (m)	Gas saturation ^b
1–8	26	0–50	M	1.00 Hz	0.15 m a	US (prior to Exp. 1)
9–16	20	20–50	M	1.00 Hz	0.15 m a	US (prior to Exp. 9)
17	26	35	M	1.00 Hz	0.15 m a	SS (prior to Exp. 17)
18–24	32	20–50	M	1.00 Hz	0.15 m a	SS (prior to Exp. 18)
25	26	35	S	0.65 s T_p	0.5 m H_s	US (prior to Exp. 25)
26	26	40	S	1.00 s T_p	0.5 m H_s	
27–34	26	10.6–50	S	1.00 s T_p	0.15 m H_s	
35	32	20	M	1.00 Hz	0.15 m a	SS (prior to Exp. 35)
EQ ^c	—	10	S	0.65 s T_p	0.15 m H_s	—

^a M = Monochromatic; S = JONSWAP spectral.

^b US = Undersaturated; SS = Supersaturated.

^c EQ = Equilibration period.

Inlet-ward of the midtank panel, we placed a cross-pattern array of five Senix ToughSonic ultrasonic distance meters (UDMs; average fetch of 7.93 m) and at a roughly similar fetch (7.71 m), a Campbell Scientific infrared gas-analyzer and 3D sonic anemometer (IRGASON). The UDMs provided time-of-flight distance to water surface data at 10–20 Hz, and the IRGASON sonic anemometer measured the u , v , and w wind velocities, and sonic air temperature T at 20 Hz. The IRGASON was placed in an off-center cross-tank position so as to not obstruct or be obstructed by other instruments. A series of three full-length (2 m) Ocean Sensor Systems (OSS) WS Type III wave wires were arranged in an equilateral triangular configuration with 0.283 m side lengths at an average fetch of 10.075 m. Each wave wire in the array recorded at 20-Hz sampling frequency and was externally hose-clamped and made taut based on visual necessity before experiments were underway. The triangular arrangement was chosen based on a similar configuration with UDMs aboard the R/V *F. G. Walton Smith* for implementation of wavelet directional method (WDM; [Donelan et al. 1996](#)) analysis using the surface elevation time series. Water surface elevation, individual wave crest statistics and feature analysis, and surface elevation spectra were derived from this array.

Above the midtank panel, two cameras were focused on a 1.20 m \times 0.90 m rectangular region of the water surface, observed through protective thin plastic sheets. Nearer to the wind inlet, a FluxData FD-1665 polarimeter comprised of a beam-splitter and three Basler Scout charge-coupled device (CCD) cameras captured images at 50 frames per second at 0°, 45°, and 90° linear polarization states for surface slope reconstruction. Details on this camera system, and its use in the laboratory and the field are described in [Laxague et al. \(2017\)](#). At the other end of the panel, a FLIR T540 series high-resolution forward-looking infrared camera was mounted to observe the surface skin temperature. The FLIR sampled nominally at about 30 Hz with 464 pixel \times 348 pixel resolution; images were saved in sequence files using FLIR Thermal Studio Pro software.

2) WATER SIDE

Water temperature was varied throughout the experiments, necessitating continuous measurements at multiple locations to ensure the water volume was homogenized. Four Decagon conductivity–temperature–depth (CTD) sensors were submerged and attached with suction cups in a downward facing orientation to give real-time information on the salinity, water temperature, heat exchanger performance for experiment timing, and depth for tank refilling. Two CTDs were placed at the fetch extremes (0.05 and 16.17 m) of SUSTAIN, near the inlet and start of the parabolic beach, respectively; the other two were positioned at 9.86-m fetch in the midtank region but at heights of 0.125 and 0.465 m above the bottom of SUSTAIN. This arrangement allowed for the calculation of horizontal and vertical gradients.

Three different instruments were submerged and attached to the bottom of SUSTAIN in the midtank region using suction cups and lead weights: an oxygen optode sensor, two

acoustic Doppler current profilers (ADCPs), and a bubble shadowgraph imager system. The oxygen optode measured O₂ concentrations and was taking measurements at the approximately 9.86-m fetch in-line with the vertically staggered CTDs. Both ADCPs were upward-sensing Nortek manufactured units; a four-beam fast-sampling Vectrino Profiler and a three-beam 2-MHz Aquadopp HR high-resolution full-depth profiler. The Vectrino Profiler provided subsurface velocity and turbulence data for this study, sampling at 100 Hz at 9.44-m fetch. Velocity and turbulence data were observed over a 0.03 m cylinder at 0.001 m vertical resolution; this field of view was 0.34 m down-fetch of the bubble imager system center.

The bubble shadowgraph imaging system (hereafter, bubble imager; [Özgökmen et al. 2018](#)) was composed of an adjustable plastic and painted steel mount and two large cylinders encasing the camera and LED light source ([Fig. 2](#)). The bubble imager was positioned underwater at 9.10-m fetch and its data transmission and power cables were fed through the midtank plywood panel to a computer. Shadowgraph images were captured with a Basler avA2300-gm area-scan camera using a telecentric lens at 5-Hz imaging frequency. The telecentric lens removes parallax error that would distort object size in the images. Using a calibration square transparency with 0.001 m \times 0.001 m grids, the 2328 pixel \times 1750 pixel field of view was translated into 0.0685 m \times 0.0515 m in physical space. Multiplied by the 0.1-m spacing between the two black cylindrical imager nodes, the bubble imager volume observed was 3.524×10^{-4} m³. The LED light source was a Luxeon Rebel royal blue (470 nm) emitter; light rays were directed through a collimator before entering the observed water volume.

3. Methods and analysis

a. Wind and surface stress

Three-dimensional air-side velocity, air density, and sonic temperature measured by the Campbell Scientific IRGASON sonic anemometer were postprocessed using a sonic diagnostic flag hierarchy described in Table 10.2 of the instrument manual (<https://s.campbellsci.com/documents/us/manuals/irgason.pdf>). Values contain a bit field monitoring various conditions pertaining to the instrument operation and data quality, each set to true until the indicated condition is no longer present. As such, bit values of “0” indicate no flags are triggered and represent good data. Velocity data were subset to retain only good values when computing measured wind speed at instrument height U_z , and for the calculation of eddy covariance momentum flux terms for determining air-side friction velocity u_* and wind stress τ . Details and equations pertaining to the friction velocity and wind stress are given in [section 4a](#).

b. Surface wave field structure and evolution

Changes in water level recorded by the aforementioned conductivity-sensitive wave wire array produced time series of water depth $d(t)$. Quality control was performed on the raw $d(t)$ to remove periodic spurious zero-value spikes caused by the power supply for the Campbell Scientific data acquisition system (DAQ) the wave wire array was wired into.

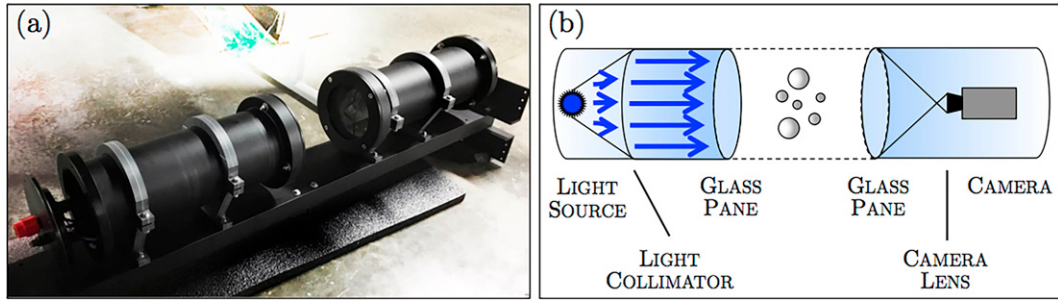


FIG. 2. The bubble shadowgraph imager (a) unit photograph and (b) components and operation diagram.

Subsequently, $d(t)$ signals were detrended accounting for water loss by spray ejection out of the SUSTAIN tank over time, yielding the water surface elevation time series $\eta(t)$. Individual wave crests and troughs were identified in each $\eta(t)$ using zero-crossing and signal peak detection algorithms. Crests and troughs were paired such that each identified wave crest had a single trough, forward edge, and rear edge. To quantify wave statistics, we adapted the aforementioned analysis techniques used on wave staff data in the SUSTAIN predecessor Air–Sea Interaction Saltwater Tank in an earlier laboratory experiment (Babanin et al. 2007). Each wave was divided into four quadrants denoted a_1 , a_2 , b_1 , and b_2 (see Fig. 3a). The height, asymmetry, and skewness of each wave was determined by mathematical relationships or ratios between the quadrants, that is,

$$H = a_1 + a_2, \quad (2a)$$

$$A_s = b_1/b_2 - 1, \quad (2b)$$

$$S_k = a_1/a_2 - 1, \quad (2c)$$

where H is the wave height in meters, A_s is the forward to rear crest asymmetry, and S_k is the above versus below zero

wave crest skewness. The (dimensionless) steepness of each crest is

$$\delta = ak = (H/2)k, \quad (2d)$$

where δ is the ratio of wave amplitude or half-height $H/2$ and wavenumber k . The wavenumber was determined by iteratively solving the gravity-capillary linear water wave dispersion relationship,

$$\omega^2 = \left(gk + \frac{\sigma}{\rho} k^3 \right) \tanh(kh) \quad (3)$$

with ω being the angular wave frequency in radians per second, g the gravitational acceleration, σ the surface tension in newtons per meter, ρ the water density in kilograms per cubic meters, and h is the water depth in meters. Once (3) is solved for k , the steepness δ , angular frequency ω , frequency f , period T , wavelength L , and celerity c were determined from linear wave theory.

In addition to omnidirectional wave crest statistics, to account for directional spread in the waves we performed wavelet directional method (WDM) using data from a triplet of

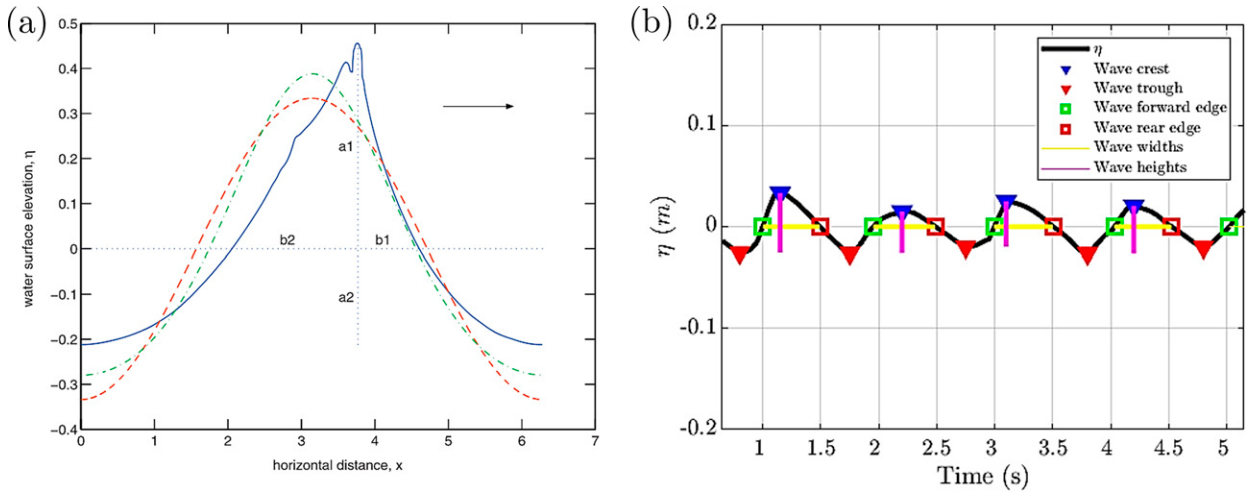


FIG. 3. Decomposition of dimensions for individual wave analysis (a) as described in Babanin et al. (2007), their Fig. 1) and (b) example based on water surface elevation η measurements from the SUSTAIN wave wire array.

wave wires in the array arranged in an equilateral triangle configuration directed toward the SUSTAIN wind-wave tank inlet. Positions, centroid, and polar angles between wires were defined and the Morlet wavelet (cf. [Donelan et al. 1996](#)),

$$\psi(t) = e^{ict} e^{-|t|^2/2} \quad (4)$$

was taken as the mother wavelet for execution of the wavelet transform. In (4), c is a constant angular wave frequency for the complex sinusoid function, $i = \sqrt{-1}$, and t is time. The wavelet transform yields time series of the amplitude and phase of each discrete frequency f given the sampling rate of the wave wire data, from which wave wire phase difference vectors ϕ_{ij} for $i, j = 1, 2, 3$ are constructed. Using WDM, we determined the directional wave spectra $S_n(\omega, \theta)$ in each wind-wave condition from the experiments with $\Delta f \approx 0.087$ Hz, $\Delta k \approx 0.187$ rad s⁻¹, and $\Delta\theta = 5^\circ$ resolution.

c. Identification of breaking waves

Breaking waves were identified by applying the phase-time processing method (PTM; [Huang et al. 1992](#); [Stansell and MacFarlane 2002](#); [Liberzon et al. 2019](#)) on the individual wave wire records of water surface elevation $\eta(t)$. Each such time series was analyzed to obtain the instantaneous frequency variations $F(t)$, which increase in the vicinity of wave crests as waves move toward breaking and steepen ([Banner et al. 2014](#); [Shemer and Liberzon 2014](#)). First, the Hilbert transform was applied to $\eta(t)$,

$$\mathcal{H}(t) = \eta(t) * \frac{1}{\pi t} = \frac{P}{\pi} \int_{-\infty}^{\infty} \frac{\eta(\tau)}{t - \tau} d\tau, \quad (5)$$

where $\mathcal{H}(t)$ is the convolution of the Cauchy kernel $1/\pi t$ and $\eta(t)$ here and P is the Cauchy principal value defining the value of the integral where improper ([Oppenheim et al. 1999](#); [Marple 1999](#)). Following this, $\mathcal{H}(t) = \eta(t) + i\xi(t)$ and the local wave amplitude $a(t) = [\eta(t)^2 + \xi(t)^2]^{1/2}$ and local wave phase $\phi(t)$ were constructed. The phase function (cf. [Liberzon et al. 2019](#)) is

$$\phi(t) = \tan^{-1} \frac{\xi(t)}{\eta(t)}. \quad (6)$$

This $\phi(t)$ was then unwrapped so that phase angle jump discontinuities of absolute magnitude greater than or equal to π were shifted to their 2π complement value, after which $\phi(t)$ was detrended. The instantaneous frequency was then calculated by differentiating the phase such that

$$F(t) = \partial\phi/\partial t. \quad (7)$$

Additional processing of $F(t)$ was subsequently performed to aid identification, namely, by applying a low-pass filter with a cutoff frequency $f_c = 5f_p$, where f_p is the peak frequency. Additionally, $F(t)$ was amplified by multiplication with $\eta(t)$ to accentuate the steeper waves, assumed to be more susceptible to breaking ([Liberzon et al. 2019](#)). A continuous Morlet wavelet was constructed and transform applied on $F(t)$, yielding the amplitude of the wavelet transform, $\|\mathcal{W}_m(f, t)\|$. This wavelet

amplitude was integrated across frequency to give the localized total wave energy $E_{lw} = \int_f \|\mathcal{W}_m(f, t)\| df$ ([Elsayed 2008](#)).

At each wave crest, a localized frequency spectrum ψ_i was found by evaluating the wavelet amplitude at the time the wave crest was observed, giving $\psi_i(f) = [\|\mathcal{W}_m(f, t)\|]_{t=t_i}$. The localized frequency spectrum $\psi_i(f)$ is used to construct the local instantaneous wave frequency F_l , which includes the raw instantaneous frequency information from $F(t)$ through the wavelet amplitude $\|\mathcal{W}_m(f, t)\|$ while accounting for wave breaking occurring in the high-frequency portion of the spectrum. The resulting F_l is

$$F_l = \left[\frac{\int_{af_p}^{f_c} f^2 \psi_i(f) df}{\int_{af_p}^{f_c} \psi_i(f) df} \right]^{1/2}, \quad (8)$$

where $\alpha = 1.35$ following [Liu \(1993\)](#) and [Elsayed \(2008\)](#). Assuming a linear dispersion relationship, waves break when the downward acceleration of the crest exceeds a limiting fraction β_0 of gravitational acceleration g such that

$$AF_l^2 \geq \beta_0 g, \quad (9)$$

where $A = 0.5H$ is the local wave amplitude or wave half-height. The value of β_0 has been assumed equal to 0.5 in classical studies ([Kinsman 1965](#)), while it has been found to be nearer to 0.4 in laboratory studies ([Hwang et al. 1989](#)), or even less than that ([Holthuijsen and Herbers 1986](#)). Following [Liu \(1993\)](#) and [Hwang et al. \(1989\)](#), we prescribe $\beta_0 = 0.4$. From (9), all wave crests across experiments were evaluated and statistics of wave breaking probability and intensity were compiled. An example comparison of 30 s of $\|\mathcal{W}_m(f, t)\|$ from monochromatic and JONSWAP spectrum wave conditions is shown in [Fig. 4](#), with localized total wave energy overlaid and symbols indicating identified breaking waves.

d. Bubble population identification and properties

Subsurface bubbles were observed using shadowgraphy, wherein the imager system camera captured the visible pattern of illumination variations caused by the refraction and reflection of light rays through and off of the bubbles. The degree of angular deflection of light by a bubble is directly related to its size and composition (i.e., void fraction) via Snell's law of refraction, $n_1 \sin\theta_1 = n_2 \sin\theta_2$, where n is the refractive index and θ is the angle of deflection relative to the interface between the two media indicated by subscripts 1 and 2.

Illumination gradients (contrast) in the images were analyzed to identify the boundaries of the bubbles via a circular Hough transform (CHT; [Atherton and Kerbyson 1999](#)), which has been used in previous studies where bubble size distribution was optically quantified ([Deane and Stokes 1999](#); [Riquelme et al. 2013](#)). For each image, the CHT uses a complex (i.e., real and imaginary) 3D accumulator array that gathers votes cast by foreground pixels of sufficient illumination gradient magnitude. A sensitivity threshold dictates whether pixels possess sufficient gradient magnitude to cast votes.

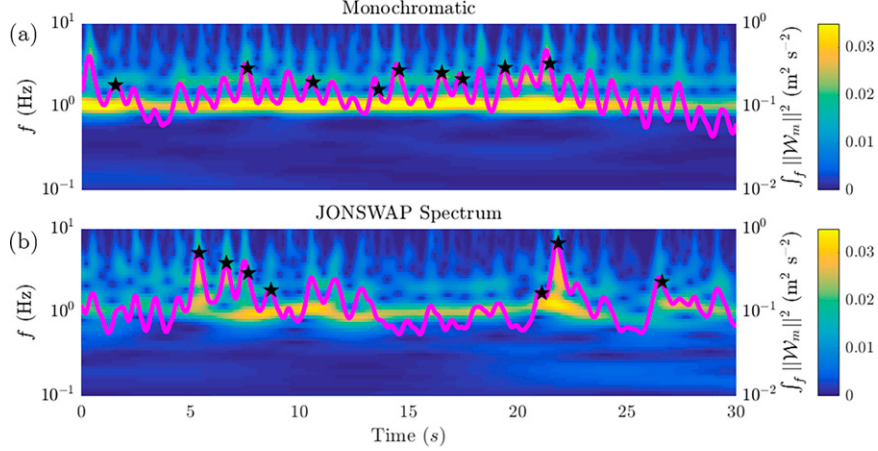


FIG. 4. Morlet wavelet amplitude $\|\mathcal{W}_m(f,t)\|$ segment for (a) monochromatic experiment 8 ($U_{10} = 35 \text{ m s}^{-1}$, $\bar{T}_w = 25.7^\circ\text{C}$) and (b) JONSWAP spectrum experiment 34 ($U_{10} = 35 \text{ m s}^{-1}$, $\bar{T}_w = 25.8^\circ\text{C}$). Overlaid is the localized total wave energy E_{lw} in magenta. The black stars, where present, are the locations of wave crests satisfying the wave crest downward acceleration breaking criterion given by Eq. (9).

Votes are cast in a circle of fixed radius r for and at the location of all eligible pixel pairs (x, y) in the images to determine the circle center (a_x, a_y) . Intuitively, overlap of votes defines the circle center and is the namesake accumulation. In a second step, the precise radius r is determined using a “phase-coding” technique; briefly, the method involves accumulating in-phase pixels along radial “spoke” lines of varying phase $0\text{--}2\pi$ radians between edge pixels and circle centers. For additional details, readers are directed to Atherton and Kerbyson (1993). For our purposes, the CHT provides coordinates of the center of bubble objects and their radii r_b over a span of radius values. Once identified, the volume V_b , surface area a_b , and void fraction estimate $\alpha_b = (V_b/V_T)$ were determined using the familiar geometric formulas by assuming spherical bubble geometry where $V_T = 3.524 \times 10^{-4} \text{ m}^3$ is the total volume observed by the bubble imager. A series of progressive bubble images showing the bubble identification process via CHT is given in Fig. 5.

Bubble size distributions (or bubble spectra) were determined by constructing a histogram using the observed bubble

radii, as in previous studies (e.g., Thorpe 1982; Deane and Stokes 2002). Bin width δr was taken to be $30.25 \mu\text{m}$, equal to the square pixel resolution of the Basler avA2300-gm area-scan camera in accordance with methodological precedent from Deane and Stokes (1999). Consequently, radii of $30.25\text{--}1512.50 \mu\text{m}$ (1–50 pixel radius) were included in size distributions. We also determined probability distribution function (PDF) and cumulative distribution function (CDF) estimates through histogram normalization.

e. Subsurface turbulence and dissipation rate

A Nortek Vectrino Profiler pulse-coherent ADCP positioned directly down-fetch of the bubble imager system was used to measure the subsurface three-dimensional velocity over a finite-depth cylinder of 0.03 m at 0.001-m vertical resolution. The ADCP sampled at 100 Hz, sufficient to resolve turbulence where an adequately dense field of subsurface scatterers was present. Individual data sequences were merged for each experiment, quality controlled, and postprocessed. Velocity data were quality controlled using measured signal-to-noise ratio

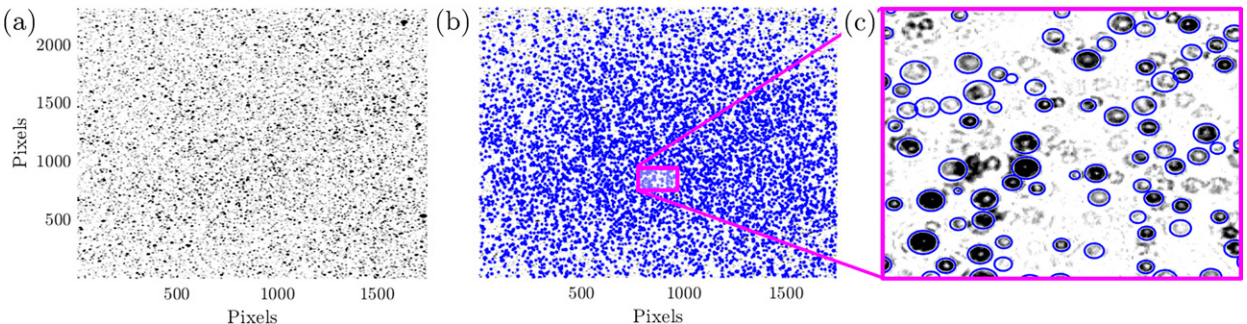


FIG. 5. Bubble identification with the circular Hough transform (CHT; Atherton and Kerbyson 1999) in an example image taken during experiment 34. (a) The raw original 2328 pixel \times 1750 pixel image, (b) identified bubble edges indicated in blue with a small inset focus on a 100 pixel \times 100 pixel section, and (c) zoomed inset showing the bubbles and labeled edges.

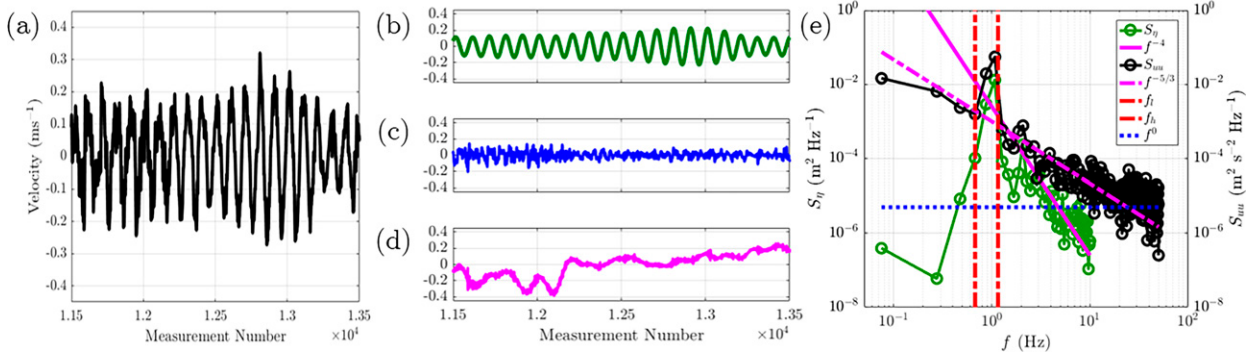


FIG. 6. Triple decomposition of subsurface velocity signals from the ADCP. (a) Raw signal u . (b) Wave-coherent signal \tilde{U} . (c) Turbulent signal u' . (d) High-frequency noise ϵ . (e) Wave (dark green) and velocity (black) spectra with the wave band identified by the red dash-dot lines and spectral slopes indicated in magenta. The blue dotted line is of zero slope.

(SNR) and a 3D phase-space despiking algorithm described in Goring and Nikora (2002). First, the SNR (cf. the Nortek Comprehensive Manual) is

$$\text{SNR}(\alpha) = 20\log_{10}\left(\frac{\|\alpha\|}{\|\alpha_\epsilon\|}\right), \quad (10)$$

where SNR has units of decibels (dB) for a velocity component α with signal amplitude $\|\alpha\|$ and noise amplitude $\|\alpha_\epsilon\|$. SNR values in the ADCP profile take a parabolic shape, with data being of good quality where $\text{SNR} \geq 20$ dB at the upper and lower ends of the vertical profile, and for $\text{SNR} \geq 30$ dB at the center of the profile.

Velocity data with SNR not meeting the relevant criteria were flagged and discarded. The Goring-Nikora 3D phase-space algorithm despiked velocity data uses a 3D phase-space or Poincaré map to separate good data from spiky data using a mathematical ellipse constructed from the derivative and Laplacian of the raw velocities. Extreme values in the derivative and Laplacian indicate outliers associated with rapidly changing data, or data with high spread or variance. Data within the Poincaré ellipse was retained, whereas spiky data was eliminated and linear interpolation was performed to fill across spikes (W. M. Drennan 2020, personal communication).

Postprocessing of velocity data consisted of the separation of mean \bar{u} , turbulent u' , and wave-coherent \tilde{u} components from the full velocity $u(t)$ where

$$u(t) = \bar{u} + u'(t) + \tilde{u}(t, \phi) + \epsilon \quad (11)$$

is the triple decomposition (e.g., Hara and Sullivan 2015; Buckley and Veron 2017) wherein t is time, ϕ is wave phase, and ϵ is high-frequency noise. Component separation was achieved following a decomposition method (cf. Benilov and Filyushkin 1970) and described in Bricker and Monismith (2007), and involved cross correlation of water surface elevation spectra S_η from wave wire data with subsurface velocity spectra S_{uu} so as to identify the wave-coherent band of the spectra. Once \tilde{u} was separated, u' was easily extracted up to a noise floor of 25 Hz (one-half Nyquist frequency) with ϵ being found as the remainder signal. An example of the signal decomposition is shown in Fig. 6.

1) THE ARIIS ALGORITHM

Dissipation rate of TKE was calculated by evaluating subsurface velocity spectra according to Kolmogorov's classical expression for the turbulence spectrum (Kolmogorov 1941),

$$S(k) = \alpha \epsilon^{2/3} k^{-5/3}, \quad (12)$$

where the Kolmogorov constant $\alpha = 0.5$ after Sreenivasan (1995), and k is the wavenumber. This expression is only valid over a subrange of the spectrum, where net energy input from large-scale eddies is in equilibrium with net energy losses to viscous or dissipation scales. This "inertial" subrange exists across a range of wavenumbers Δk (Ortiz-Suslow and Wang 2019) that has historically been identified using arbitrary bandwidths or subjective visual inspection of the velocity spectra (e.g., Large and Pond 1981; Fairall and Larsen 1986; Yelland and Taylor 1996; Sjöblom and Smedman 2002).

A recently developed algorithm for robustly identifying the inertial subrange (ARIIS; Ortiz-Suslow et al. 2020) alleviates subjective ambiguity by identifying the most probable Δk and the slope of the inertial subrange using an empirical fit. ARIIS was originally field tested using turbulent velocity data collected offshore of Southern California from towered 3D ultrasonic anemometers aboard the R/P FLIP during the Coupled Air-Sea Processes and Electromagnetic Ducting Research (CASPER; Wang et al. 2018) field campaign. ARIIS has three steps: 1) declaration of inputs and constants, 2) check for isotropic convergence, and 3) robust slope-fitting of the identified subrange to $k^{-5/3}$.

Isotropic convergence is tested using an isotropy coefficient I_{ij} (Jimenez et al. 1993) and searching across all k between the declared low wavenumber limit and high wavenumber tail truncation point. The coefficient converges to unity over an isotropic wavenumber space (i.e., $I_{ij} \rightarrow 1$) and is defined

$$I_{ij}(k) = \frac{E_{ii}(k) + k(\partial E_i / \partial k)}{2E_{jj}}, \quad (13)$$

where i and j are orthogonal velocity components from the set $U = \{u, v, w\}$ and $E(k)$ (taking subscripts i, j) are the observed velocity spectra. Subsequently, ARIIS routines flag and

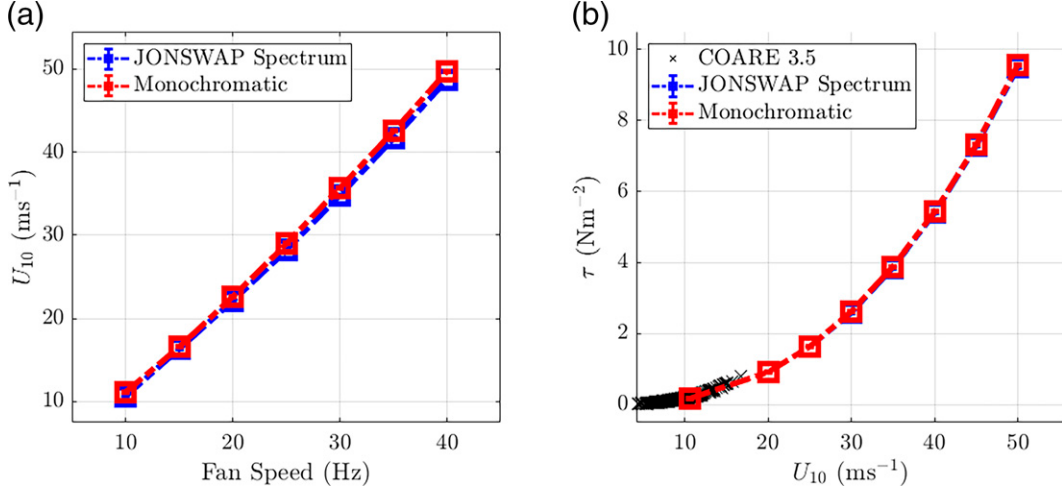


FIG. 7. Wind and stress in SUSTAIN experiments with monochromatic and JONSWAP spectrum wave conditions: (a) 10-m equivalent wind speed U_{10} as a function of SUSTAIN fan speed (Hz) and (b) τ (N m^{-2}) as a function of U_{10} . COARE 3.5 data (Edson et al. 2013) are given by the black crosses.

discard Δk that are too broad, where no subrange exists that satisfies (12), or for which there was not isotropic convergence. Once the inertial subrange is defined, (12) is solved for turbulent kinetic energy (TKE) dissipation rate ε ,

$$\varepsilon = \alpha^{-3/2} k^{5/2} S(k)^{3/2}. \quad (14)$$

We then invoke an extension of Taylor's frozen turbulence hypothesis $k = 2\pi f U_a^{-1}$ (Taylor 1938) for unsteady advection (Lumley and Terray 1983; Terray et al. 1996; W. M. Drennan 2020, personal communication) where $U_a = \sqrt{2\bar{w}^2}$ is the advection or drift velocity of turbulence by the waves past the (stationary) ADCP. As in all cases the RMS wave velocity exceeded the mean velocity \bar{u} by between 2 and 3.5 times, this "surrogate" (unsteady) advection velocity is used in place of the conventional advection velocity, $\bar{u} = u - u'$, to arrive at ε in terms of the subsurface along-flow (i.e., zonal) velocity spectrum $S_{uu}(f)$. We note that our choice of advection velocity, although physically based, results in turbulent kinetic energy dissipation ε values that vary by 12.1%–18.5% beneath our JONSWAP spectrum wave cases and 14.1%–20.8% beneath our monochromatic wave cases versus those determined via the conventional definition of advection velocity. For each segment of velocity data, the validity of Taylor's frozen turbulence hypothesis was ascertained via a nondimensional ratio of turbulence intensity and advection velocity,

$$\xi = |w'|/|U_a|, \quad (15)$$

where (14) is valid for $\xi \ll 1$, such that TKE dissipation rates for which $\xi \geq 0.5$ were discarded.

4. Results

a. Wind stress and surface wave spectra

In each experiment described in Table 1, mechanically driven paddle waves featuring monochromatic or JONSWAP

spectrum frequency distribution were generated continuously while fan-driven winds were smoothly conveyed overtop the water surface. Figure 7 shows the 10-m equivalent wind speed U_{10} and wind stress τ in the two wave types as a function of the fan speed and U_{10} , respectively. U_{10} was calculated assuming neutral stability via

$$U_{10} = U_z + \frac{u_*}{\kappa} \log\left(\frac{10}{z}\right), \quad (16)$$

where U_z is the wind speed at sonic anemometer height $z \approx 0.59$ m in SUSTAIN, u_* is the air-side friction velocity, and $\kappa = 0.41$ is the von Kármán constant. Wind stress τ was calculated using eddy covariance of turbulent velocity components measured by the Campbell Scientific IRGASON sonic anemometer,

$$\tau = \rho_a u_*^2 = \rho_a (-\overline{u'w'}^2 - \overline{v'w'}^2)^{1/2}, \quad (17)$$

and surface corrected using an air-side momentum budget approach [cf. Donelan et al. 2004, see their Eq. (5)] involving relating the horizontal air pressure gradient $\partial p/\partial x$ to the vertical gradient of wind stress $\partial \tau/\partial z$ to solve for surface stress, performed separately from our laboratory experiments in the SUSTAIN facility [Curcic and Haus 2020, see also their Eq. (1)].

Laboratory fan speeds ranged from 11.0 to 40.9 Hz, producing $U_{10} = 11\text{--}50$ m s⁻¹ (24.6–111.8 mph) or category 3 equivalent at the highest fan speed used. As wind speed measured inside SUSTAIN is dependent upon both fan speed and air volume constriction from changes in water depth (e.g., wave propagation, water loss due to spray ejection), U_{10} was 1.4%–2.5% larger in the presence of monochromatic waves versus when JONSWAP spectrum waves were present. The τ increased in the presence of both wave types, with a quadratic to linear dependence on U_{10} . Differences in wind stress measured above the two wave types increased according to a

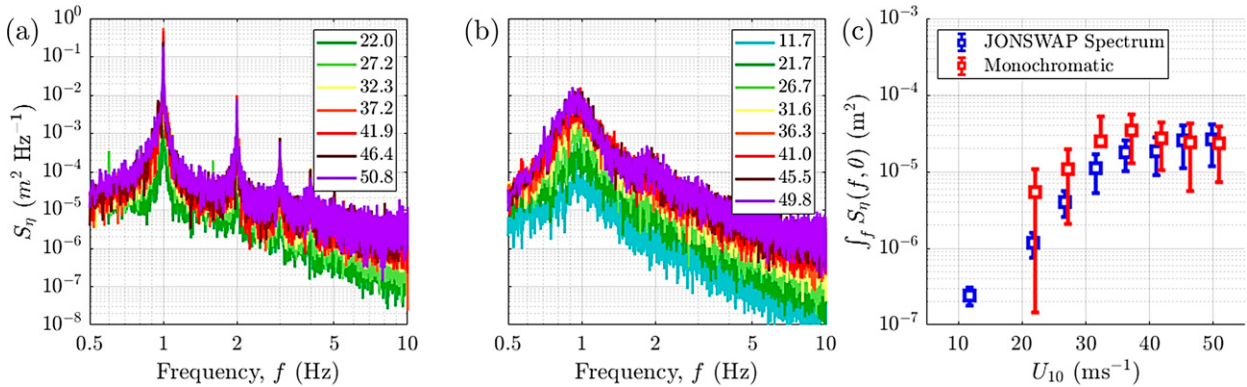


FIG. 8. Water surface elevation (wave) spectra from (a) experiments 2–8 with monochromatic wave field present, and (b) experiments 27–34, where JONSWAP spectrum waves were present. (c) Integrated directional wave spectral density: compare the monochromatic (red) and JONSWAP spectrum (blue) wave spectra. Each value in (c) considers wave energy from $\pm 30^\circ$ from the wave propagation direction (down-fetch). Squares indicate the mean while the error bars give ± 1 standard deviation.

quadratic fit with U_{10} from $\Delta\tau \approx 0.0067$ – 0.0682 N m^{-2} , with τ larger above monochromatic waves than JONSWAP spectrum waves. Consequently, 2.0%–4.1% less aerodynamic drag C_{D10} is observed above monochromatic waves.

Water surface elevation (wave) spectra $S_\eta(f)$ constructed from $\eta(t)$ are presented in Fig. 8, color-coded according to increasing U_{10} . Here, we compare S_η from monochromatic wave experiments 2–8 to those from JONSWAP spectrum wave experiments 27–34, where fan speed and starting water levels were the same and average water temperatures T_w were 25.7° and 25.9°C, respectively. In both sets of experiments, the dominant wave is swell-like with average peak frequency of $0.9997 \pm 0.0012 \text{ Hz}$ and $0.9556 \pm 0.0276 \text{ Hz}$ in Figs. 8a and 8b, respectively, with each spectrum showing evidence of bound wave harmonics at multiples of the peak. Bound waves, generated by dominant long waves, have been commonly observed in short-fetch wind-wave tanks particularly where the amplitude of the dominant wave is large (Plant et al. 1999, 2004; Laxague et al. 2017). In Fig. 8c, the integrated wave spectral density is shown to summarize the spectra. For both wave conditions, the integrated wave spectral density increases with wind speed until $U_{10} \approx 37 \text{ m s}^{-1}$. As wind speed

increases further, integrated wave spectral density decreases and levels off in monochromatic wave conditions, whereas the integrated spectral density takes a more concave shape although still increasing for JONSWAP spectrum wave conditions. The variance of the integrated wave spectral density increases with U_{10} for JONSWAP spectrum paddle wave conditions, while in monochromatic wave conditions, the smallest variance is observed at a transition wind speed of $\approx 37 \text{ m s}^{-1}$. The integral in Fig. 8c is proportional to significant wave height H_{sig} , indicating the wave heights of monochromatic waves are statistically larger than those from the JONSWAP spectrum wave field for $U_{10} \leq 37.2 \text{ m s}^{-1}$.

b. Surface wave statistics

By individually analyzing wave crests captured by wave wire data using the aforementioned zero-crossing wave quadrant method (cf. Babanin et al. 2007), we quantified statistics of the waves observed in each experiment. Figure 9 summarized the statistics, including wave frequency f , wavenumber k , wave height H , wave steepness $\delta = (H/2)k$, above–below zero wave skewedness S_k , and forward–rear wave crest asymmetry A_s . In each panel, we color the data according to significant wave

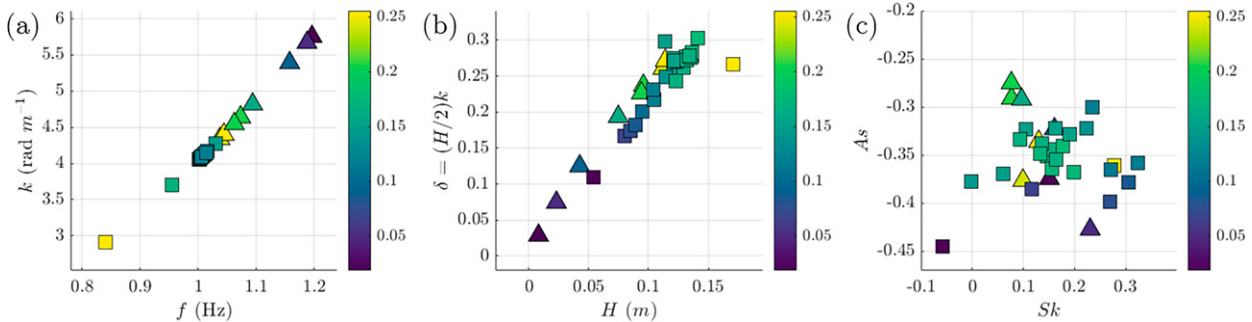


FIG. 9. Wave statistics determined from SUSTAIN wave wire data. (a) Median wavenumber k and wave frequency f . (b) Median wave height H and steepness δ . (c) Median wave crest skewedness S_k and wave crest asymmetry A_s . In each panel, monochromatic wave statistics are indicated by squares, while JONSWAP spectrum wave statistics are indicated with triangles. Each data point across all panels is colored according to significant wave height H_{sig} given by the color bar.

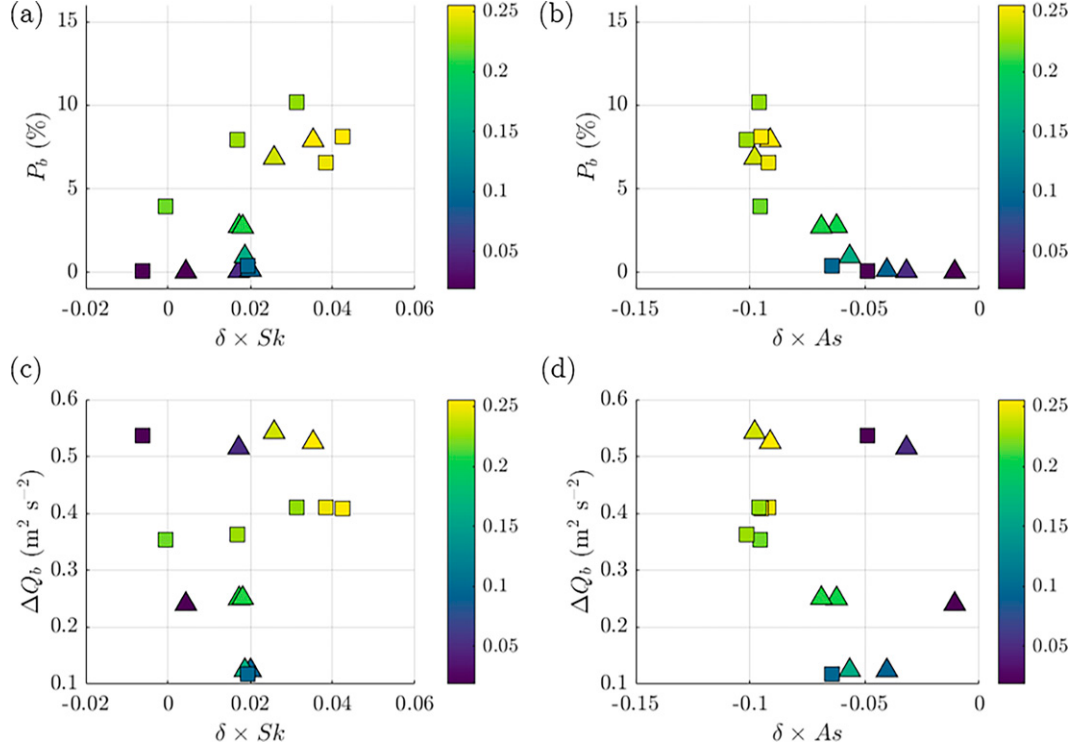


FIG. 10. (a),(b) Wave breaking prevalence and (c),(d) kinetic energy loss due to breaking as a function of (left) steepness scaled skewedness $\delta \times S_k$ and (right) steepness scaled asymmetry $\delta \times A_s$. In each panel, monochromatic wave statistics are indicated by squares, while JONSWAP spectrum wave statistics are indicated with triangles. Each data point across all panels is colored according to significant wave height H_{sig} given by the color bar.

height H_{sig} . In each panel, statistics from monochromatic wave (JONSWAP spectrum wave) experiments are indicated with squares (triangles). In Fig. 9a, waves of higher frequency f have higher wavenumber k regardless of wave condition; however, waves in monochromatic conditions are substantially more clustered around $f = 1.00$ Hz and $k = 4.00$ rad m^{-1} . Average frequency and wavenumber for these monochromatic cases was $\bar{f}_M = 0.99 \pm 0.04$ Hz and $\bar{k}_M = 4.03 \pm 0.26$ rad m^{-1} , respectively, with a relatively modest inverse correlation between f or k and H_{sig} ($R^2 = -0.51$). In contrast in the JONSWAP spectrum wave experiments, f and k decrease monotonically with H_{sig} with strong inverse correlation ($R^2 = -0.99$). Thus, monochromatic waves possessed little frequency or wavenumber variance whereas JONSWAP spectrum waves clearly become longer (frequency downshift) and higher (greater H_{sig}).

Wave steepness shows similar behavior in Fig. 9b in that, although wave height and steepness increase expectedly with H_{sig} , JONSWAP spectrum waves steepen 4.5% faster per unit wave height than the monochromatic waves. Monochromatic waves, however, again have greater average steepness and less spread in δ values, with $\bar{\delta}_M = 0.24 \pm 0.05$ versus $\bar{\delta}_J = 0.18 \pm 0.09$ in JONSWAP spectrum conditions.

Laboratory and numerical model investigation into predicting breaking wave onset (Babanin et al. 2007) and results from earlier wave breaking studies (Cauliez 2002; Young and Babanin 2006) have measured inherent nonlinear characteristics of breaking

waves, namely, the asymmetry and skewedness. Figure 9c shows measurements for these two wave crest features, and from cursory examination the relationship is less clear than the previous statistics. Based on their definitions in (2b) and (2c), breaking of waves is favored where asymmetry is negative (wave crest tilted forward in direction of propagation) and where skewedness is positive (crest height exceeds trough depth). In Babanin et al. (2007), these behaviors occur with increasing wave steepness δ (see their Fig. 4).

In Fig. 9c, monochromatic waves actually become less negatively asymmetric (although $A_s < 0$) and less positively skewed (although $S_k > 0$) as they steepen, with a weak trend ($R^2 = -0.21$) of decreasing A_s with increasing S_k . Conversely, for JONSWAP spectrum waves experiments there are two behaviors dependent upon wave steepness δ : for small to moderate δ , asymmetry and skewedness of waves is less negative and less positive, respectively; for moderate to large δ , wave crests asymmetry becomes increasingly negative and skewedness becomes increasingly positive. Additionally, the correlation of wave crest asymmetry A_s and skewedness S_k in JONSWAP spectrum experiments is large and significant ($R^2 = 0.76$, $p_{0.05} = 0.016$) where $p_{0.05}$ is the significance test probability at the 95% confidence interval. The inflection point between these two behaviors occurs at $\delta = 0.23$ where $U_{10} \approx 36$ m s^{-1} , suggesting that JONSWAP spectrum waves may break as a consequence of the effects of

TABLE 2. Brief summary of several field, numerical, and laboratory studies involving the measurement of bubble size distributions including the present work, with units where necessary indicated. In the table, H refers to wave height, T to wave period, T_w to water temperature, PB to plunging breaking waves, SB to spilling breaking waves, MWP to mechanical wave packet, WPF to wave packet frequency, and NPS to natural pumped seawater.

Publication	Type ^a	Wind (m s^{-1})	Waves	Environment	Bubble sizes (μm)
Blanchard and Woodcock (1957)	F	Onshore Coastal	Breaking Shallow water	$T_w \approx 21^\circ\text{C}$	80–100
Medwin (1970)	F	—	$H \approx 0.5\text{ m}^{\text{b}}$	$T_w \approx 17^\circ \pm 0.1^\circ\text{C}$	20–125
Medwin (1977)	F	3.3–6.1	$H \approx 0.6\text{--}2.0\text{ m}$	—	25–250
Johnson and Cooke (1979)	F	8.0–13.0	$H \approx 2.0\text{ m}, T \approx 3\text{--}4\text{ s}$	$T_w \approx 3^\circ\text{C}$	75–200
Thorpe (1984)	N	—	—	—	30–180
Deane (1997)	F	3.0–5.0	$H \approx 0.9\text{ m}, T \approx 7\text{ s}$	$T_w \approx 18^\circ\text{C}$	50–1000 ^c
Deane and Stokes (1999)	F	3.0–5.0	$H \approx 0.9\text{ m}, T \approx 7\text{ s}$	$T_w \approx 18^\circ\text{C}$	200–1100
Deane and Stokes (2002)	L	None	$H \approx 0.1\text{ m}$ PB MWP $\text{WPF} \approx 0.73 \pm 1\text{ Hz}$	—	100–1000 ^c
Callaghan et al. (2014)	L	None	PB sheet-like jets	$T_w \approx 5^\circ\text{--}30^\circ\text{C}$	40–500
Deane et al. (2016)	L	None	$H \approx 0.2\text{--}0.8\text{ m}$ MWP SB, PB	NPS	200–4000
Present Study	L	11.2–53.5	$H \approx 0.15\text{--}0.5\text{ m}$ $T \approx 0.65\text{--}1.0\text{ s}$	$T_w \approx 19.9^\circ\text{--}32.4^\circ\text{C}$ NPS	30–1500

^a Field (F), numerical (N), or laboratory (L).

^b WMO sea state 1–2.

^c Range of 90+ % of obs.

nonlinear asymmetries, while monochromatic wave breaking is occurring as a consequence of steepness of the waves. Monochromatic wave breaking may also be augmented by the presence of bound waves on the leeward face more commonly observed with higher-amplitude long waves (Plant et al. 1999).

Wave breaking likelihood P_b is quantified using the dynamic criterion (Hwang et al. 1989; Liu 1993) given in (9), relating downward acceleration of wave crests to gravitational acceleration, in both monochromatic and JONSWAP spectrum wave experiments (Fig. 10). In Figs. 10a and 10b, the wave steepness δ is multiplied by skewedness and asymmetry, respectively, to represent cumulative effects of steep and asymmetric waves. In Figs. 10c and 10d, steepness scaled skewedness and asymmetry are related to the kinematic energy loss due to breaking estimated via $\Delta Q_b = u^2 + w^2$, where u and w are particle velocities at the free surface, following Hwang et al. (1989). Recapitulating, positive skewedness and negative asymmetry are associated with breaking, and feature crests larger above the zero vertical plane with forward tilt in the direction of wave propagation (Babanin et al. 2007). In Fig. 10a, breaking likelihood is found to increase as waves steepen and crests are skewed positive. Linear regression fits of P_b and $\delta \times S_k$ show statistical significance in JONSWAP spectrum conditions at 95% confidence ($R^2 = 0.66, p_{0.05} = 0.014$), while correlation and p values for the monochromatic cases were lower and not significant at equal confidence ($R^2 = 0.46, p_{0.05} = 0.09$). Conversely, increasingly negative steepness scaled lateral crest asymmetry $\delta \times A_s$ is statistically significantly correlated with larger P_b in both wave conditions ($R^2 = 0.82, p_{0.05} = 0.002$, and $R^2 = 0.75$, in JONSWAP spectrum and monochromatic experiments, respectively).

Kinematic energy loss ΔQ_b has no significant relationship with steepness scaled skewedness $\delta \times S_k$, however, statistical significance is observed when coupling the effects of steepness

and lateral asymmetry via $\delta \times A_s$. In both JONSWAP spectrum and monochromatic wave experiments, increased scaled asymmetry results in larger energy loss due to breaking, with $R^2 = 0.92, p_{0.05} = 0.002$ and $R^2 = 0.84, p_{0.05} = 0.010$, in the respective conditions. Summarizing, we observe increased wave breaking likelihood with steeper, positively skewed, and negatively asymmetric waves; particularly, correlations and significance statistics are most similar when considering the relationships between wave crest asymmetry, breaking likelihood, and wave breaking intensity (via the proxy ΔQ_b). Hence, the combined effects of steepness and asymmetry are the most universal across our observed wind and wave conditions in the context of breaking probability and intensity.

c. Bubble size distributions

Bubble populations have been estimated or quantified by visual, camera-aided optical, and acoustic methods since the mid-twentieth century; therefore, we first summarize wind, wave, notable environmental conditions, and bubble size to contrast data from prior studies with those in this work in Table 1.

From Table 2, we note the earlier studies were field experiments in coastal locations, offshore of beaches, and from research vessels or platforms; however, this summary table does not report all extant studies. More recent work has been conducted in controlled laboratory settings and has included expanding the upper range of observed bubble radii using improved acoustic and optical methods as well as via the benefit of larger tanks and fetch. Our study includes the highest range of wind speeds and the only to attain hurricane-force intensity, two distinct types of waves (the use of mechanical wave paddles is not unique to our work), and natural seawater as in Deane et al. (2016). We also observed a wide range of radii in the bubbles seen, taking advantage of high pixel resolution

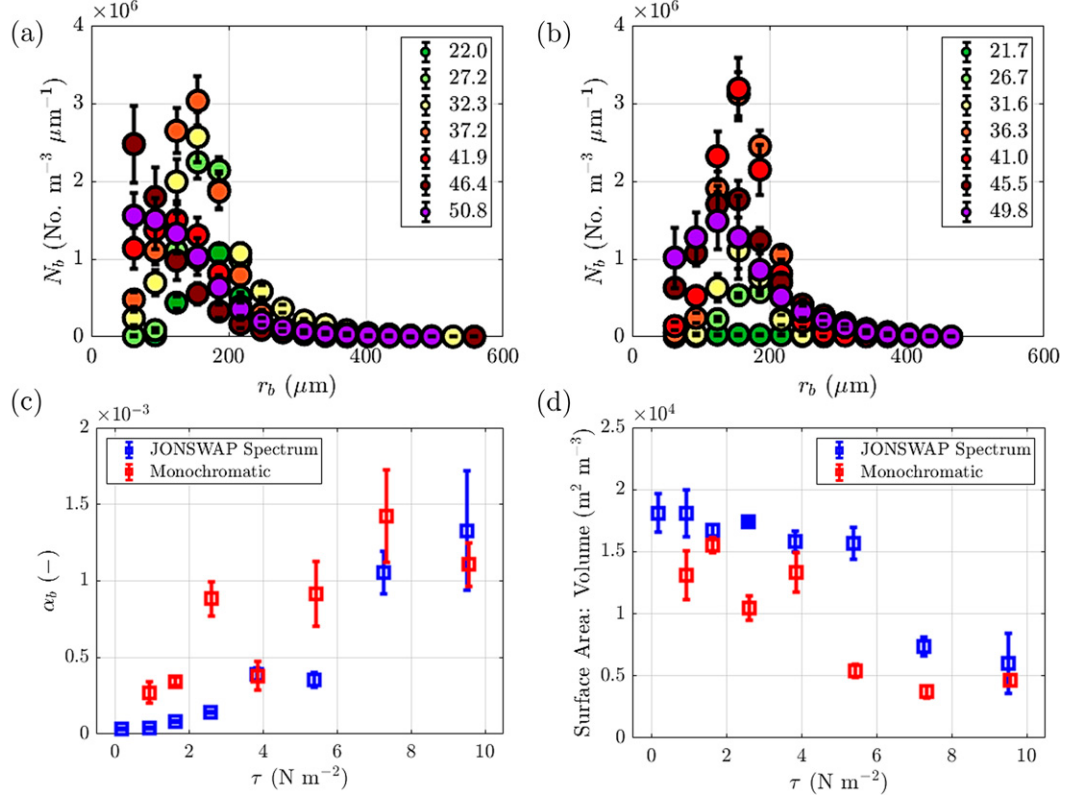


FIG. 11. Bubble size distributions for (a) monochromatic experiments 1–8 and (b) JONSWAP spectrum wave experiments 27–34, color-coded by U_{10N} . Colored circles indicate the bin average, and error bars show 1 standard deviation across the 10 images used in the construction of each distribution. (c) Void fraction α and (d) surface area to volume ratio for the respective experiments as a function of wind stress τ , defined in Eq. (17).

in a subsurface optical system (shadowgraph imager) and robust bubble identification algorithm (Atherton and Kerbyson 1999; see also Deane and Stokes 1999; Riquelme et al. 2013).

We fit observed bubble size distributions using an exponential distribution valid from the peak radius to the maximum observed radius. This choice captures the peak magnitude and fall-off (high-radius tail) of the bubble size distributions, which are connected to the surface wind forcing and wave conditions above. Given that the likelihood of observing bubbles of a given radius decreases with size due to buoyant outgassing, the exponential distribution was a prudent choice for our purposes. Using maximum likelihood estimation (MLE; Dempster et al. 1977), the peak and spread of the distributions can be captured. By normalizing radius and bubble density (bubbles per volume per radius micron), between the peak radius and some high-radius limit any bubble size distribution can be described via the exponential function,

$$n(r) = N_{\text{peak}} \exp^{-\gamma r}, \quad (18)$$

where N_{peak} is the number of bubbles observed at the peak of the distribution, γ is a bubble loss or decay rate, and r is the bubble radius, respectively. The N_{peak} statistically describes

the prevailing size of bubbles, and γ is inversely proportional to the spread, diversity, or variety of bubble sizes.

In the present study, bubble size distributions were constructed from a series of 10 shadowgraph images taken beneath the water surface and temporally in the middle of each experiment. We focus on the bubble density beneath the monochromatic and JONSWAP spectrum wave experiments 1–8 and 27–34, respectively. In these experiments, 10-m equivalent wind speed $U_{10N} = 11.2\text{--}53.5 \text{ m s}^{-1}$ and average water temperature $\bar{T}_w = 25.72^\circ \text{ and } 26.01^\circ\text{C}$, respectively. Figures 11a and 11b show the average bubble density $N_b = \text{No. m}^{-3} \mu\text{m}^{-1}$ (cf. 10 shadowgraph images in each experiment) scaled to reflect statistics from a water volume of 1 m^3 (recall, the observed water volume in SUSTAIN was $3.52 \times 10^{-4} \text{ m}^3$).

Average bubble size distributions, regardless of wave conditions present, show an increase in the total number of bubbles over low to moderate $U_{10N} \approx 11.7\text{--}34.8 \text{ m s}^{-1}$. The number of bubbles beneath JONSWAP spectrum (monochromatic) waves increases by approximately 4.6 times (2.4 times) at a rate of about $\Delta n / \Delta U_{10} \approx 5.75 \times 10^5$ (1.22×10^6) bubbles (m s^{-1}) $^{-1}$, followed by a decrease in the number of bubbles at higher winds. Therefore, monochromatic waves produce a greater number of bubbles at a greater rate with the increase

in wind forcing at these speeds. Additionally, while the peak (or most observed) bubble radius is steady or increasing over the low to moderate wind speeds, for $U_{10} > 35 \text{ m s}^{-1}$ the peak bubble radius decreases in both wave conditions. Beneath JONSWAP spectrum (monochromatic) wave conditions, this occurs at a rate $\Delta r/\Delta U_{10} \approx -7.2$ (-6) $\mu\text{m}/\text{m}$. Therefore, subject to comparable wind speeds and marginally higher stress ($\overline{\tau_M}/\overline{\tau_S} \approx 1.007$), bubble size decreases 7.5% faster with 1.7 times greater variance in observed bubble radius beneath the monochromatic waves, which are 23.0% steeper, 13.3% more laterally asymmetric, and have 39.8% larger breaking intensity as estimated by ΔQ_b .

In Figs. 11c and 11d, we show the void fraction $\alpha_b = (V_b/V_T)$ and surface area to volume ratio (SA:V), respectively, for the same experiments whose bubble number spectra are shown in Figs. 11a and 11b. Although void fraction magnitude is on average 3.2 times larger in monochromatic wave conditions than JONSWAP spectrum wave conditions, void fraction increases 1.5 times faster beneath the latter wave condition. Surface area to volume ratio, which relates the exposed bubble surface given a certain internal volume (shown in Fig. 11d), indicates a greater magnitude of SA:V in JONSWAP spectrum wave conditions. SA:V is 1.6 times larger in JONSWAP spectrum wave conditions; however, the reduction in SA:V with stress occurs at a rate 4.7 times as quickly in monochromatic conditions. Therefore, larger total entrained bubble volume results in greater void fractions in monochromatic wave conditions where waves are higher, steeper, and more frequently break. Conversely, in monochromatic conditions a more rapidly decreasing bubble radius and SA:V with increasing stress demonstrate the greater number of small bubbles observed in monochromatic wave condition bubble spectra.

To parameterize bubble size distributions, we consider that air-sea gas transfer is facilitated through a vertical flux between the atmosphere and ocean. Wind speed and wave state both contribute to the efficacy of transfer and amount of air entrainment (Brumer et al. 2017). We quantified the void fraction, the number of bubbles, and the radius of those bubbles via the aforementioned CHT algorithm (Atherton and Kerbyson 1999). Each bubble statistic was evaluated in terms of the energy flux from wind to waves per unit water density (Drennan et al. 1996; Terray et al. 1996),

$$F = g \int_0^{2\pi} \int_0^\infty \beta S_\eta d\omega d\theta, \quad (19a)$$

where g is the gravitational acceleration, $S_\eta(\omega, \theta)$ is the directional wave spectrum, and β is the wave growth rate (cf. Terray et al. 1996),

$$\beta = 0.194 \left(\frac{\rho_a}{\rho_w} \right) \left[\frac{U_{\pi/k} \cos \theta}{c(k)} - 1 \right] \left[\frac{U_{\pi/k} \cos \theta}{c(k)} - 1 \right] \Big|_\omega, \quad (19b)$$

where 0.194 is the Jeffreys sheltering coefficient (Jeffreys 1924, 1925) taken to be a constant (Larson and Wright 1975); ρ_a and ρ_w are the air and water densities, respectively; c is the wave phase speed; ω is the wave angular frequency; θ is the

difference in wind and wave propagation direction; and $U_{\pi/k}$ is the wind speed at half-wavelength height via

$$U_{\pi/k} = U(z) + (u_*/\kappa) \ln[\pi/(kz)]. \quad (19c)$$

Each F is scaled by the measured significant wave height H_{sig} , with units of energy per unit mass per unit time (W kg^{-1}).

Void fraction α_b increases exponentially and statistically significantly with FH_{sig}^{-1} ($R^2 = 0.84$, $p_{0.05} = 0.000167$), representing the increase in air entrainment with wind input relative to the wave height. It is clear from Fig. 8c that in high winds the wave energy and subsequently the significant wave height either level off or decrease, so the largest void fractions are consistent with the greatest wind energy input occurring at high winds per unit of wave height which is diminished via a combination of wave crest tearing and breaking. The total number of bubbles observed in any distribution was also found to be significant, increasing linearly with FH_{sig}^{-1} ($R^2 = 0.85$, $p_{0.05} = 0.000146$). The number of bubbles is strongly related to significant wave height, in that the bubble plume depth is in part determined by the volume of the initial air cavity (Deane and Stokes 2002) as the wave breaks. Finally, we considered the average radius of the bubbles. Although the depth of the bubble plume from the surface above it is approximately 0.30 m and the turbulent bubble cascade within actively breaking wave crests is not expected to be observed, bubble radius statistically significantly decreases with FH_{sig}^{-1} ($R^2 = 0.78$, $p_{0.05} = 0.000149$). We expect that with increasing wave-scaled wind input FH_{sig}^{-1} that larger entrainment velocities inject bubbles into the view of the bubble imager leaving smaller bubbles as those of larger radius rapidly buoyantly outgas. It may also be that greater subsurface turbulence from breaking waves results in the loss of larger bubbles before they are observed by imager; however, since we do not image the entire subsurface water the entire fate of individual bubbles is not known from injection onward. Overall, the amount of air entrainment and subsequent number of bubbles observed are linked to the increased roughness and height of waves—each of which are factors influencing the frequency and intensity of wave breaking. The size of bubbles observed are seen to decrease as the wind-wave conditions become rougher and subject to larger momentum flux.

A series of bubble images, each with progressively larger FH_{sig}^{-1} , are shown in Fig. 12 to visually compare behavior of the bubbles beneath the monochromatic and JONSWAP wave spectrum wind-wave environments. Each image is colorized such that bubbles appear as blue and ambient water volume appears as yellow. In both wave conditions, bubbles are at first spaced apart in the images and some larger bubbles (a minority) can be clearly seen. As FH_{sig}^{-1} increases, the smaller bubbles become more numerous, and groups of bubbles are seen clumping together. By the time the highest wind speeds are reached in either wave condition, the bubble image field is composed of groups of bubbles together and irregular fragments of dark and light area are seen in the images. By this point, bubbles are interacting with each other below the water surface and the images are saturated with bubble clusters.

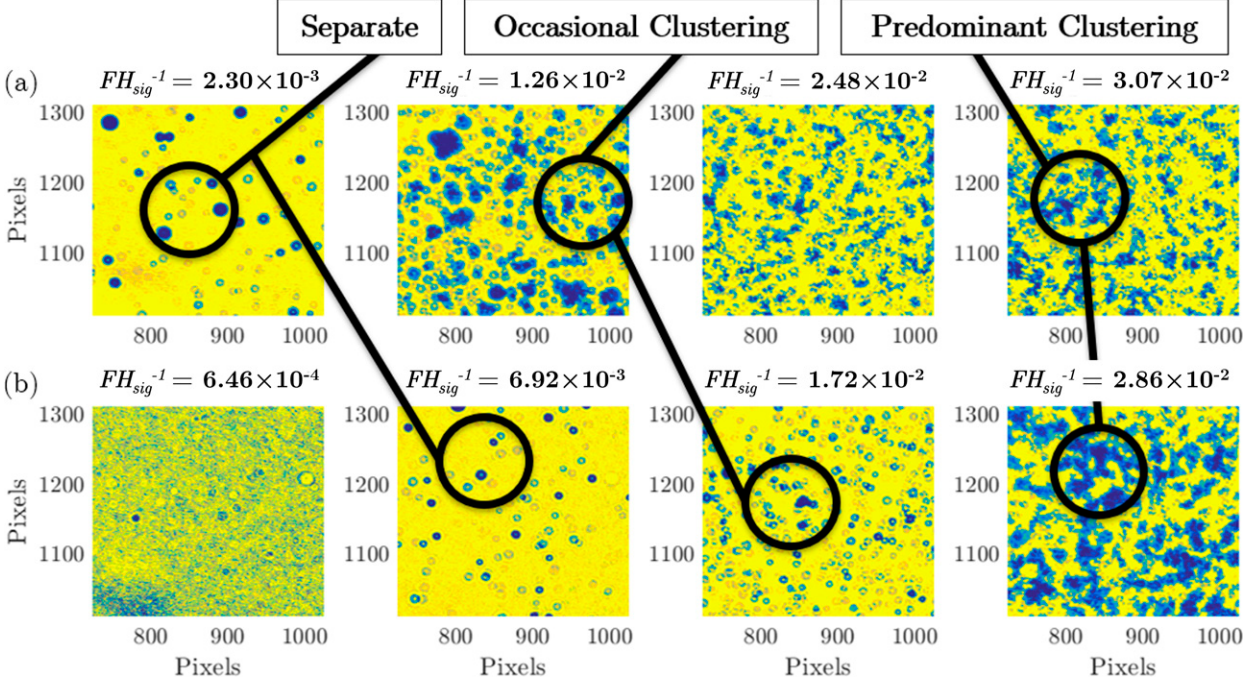


FIG. 12. Subsurface bubble evolution and interaction as captured in shadowgraph images subject to increasing FH_{sig}^{-1} (W kg^{-1} or $\text{m}^2 \text{s}^{-3}$) in (a) monochromatic and (b) JONSWAP spectrum wave conditions. All axis dimensions are pixels (each image 2328×1750 pixels).

d. Parameterization of bubble distributions based on wind, wave, and temperature data

The two parameters of the exponential distribution (N_{peak} and γ) were determined for both monochromatic and JONSWAP spectrum wave conditions and expressed in terms of wave-scaled wind input to waves FH_{sig}^{-1} in Fig. 13. We describe the evolution of these parameters in terms of what was seen in the bubble images according to FH_{sig}^{-1} in Fig. 12, that is, in terms of separate growth, occasional, and finally saturated clustering of bubbles. For $FH_{\text{sig}}^{-1} < 5 \times 10^{-3} \text{ W kg}^{-1}$, N_{peak} and γ both increase; the average number and size of bubbles increases, but the bubble population remains narrow (growth, formation of bubbles). Over moderate $FH_{\text{sig}}^{-1} \approx 5 \times 10^{-3}$ – $2 \times 10^{-2} \text{ W kg}^{-1}$, some groups of larger bubbles group together while many individual bubbles remain free or separate (occasional clustering). Regardless of wave condition, here, the bubble size distribution broadens to include more bubble radii and increasingly smaller bubble sizes (N_{peak} decreases and γ increases). At $FH_{\text{sig}}^{-1} > 2 \times 10^{-2} \text{ W kg}^{-1}$, depending on wave condition, the field of view of the bubbles becomes bright and quite saturated (see Fig. 12). Here, the bubble size distributions continue to broaden, and the average bubble size continues to decrease. We hypothesize the degree of clustering and saturation in images are directly related to the presence of wave-induced subsurface turbulence shearing apart bubbles and that small bubbles or fragments of bubbles clump together due to the cohesive properties of the water. In Fig. 13, the black dashed lines show the best fits between the distribution parameters and wave-scaled wind input taking the form

$$\gamma \approx a_0 FH_{\text{sig}}^{-1} - b_0, \quad (20a)$$

$$N_{\text{peak}} \approx a_1 \exp(\gamma b_1), \quad (20b)$$

where $a_0 = 0.467$, $b_0 = 0.02436$, $a_1 = 5.36 \times 10^4$, and $b_1 = -363.3$.

To validate the parameterizations and quantify error, the average of 10 distributions (one per shadowgraph image) were compared with constructed exponential distributions using the expected values defined via (2a) and (2b). Histograms of the observed distributions beneath JONSWAP spectrum waves are overlaid with both the parameterized exponential distribution using FH_{sig}^{-1} and the exact exponential fit in Fig. 14. Given in the legends are the ratios N_p/N_m , the ratio of the parameterized and measured number of bubbles at the peak of the distribution, and γ_m/γ_p , a similar ratio for the bubble radius decay rate.

In Fig. 14, parameterized bubble size distributions agree well with observations at wind speeds $U_{10} \geq 31.6 \text{ m s}^{-1}$, with N_p/N_m and γ_m/γ_p nearer to unity in those cases. The most commonly observed bubble radius observed as indicated by the peaks in $n(r)$ decreases from $r = 166 \mu\text{m}$ to $r = 75 \mu\text{m}$ as wind speed increases from 31.6 to 49.8 m s^{-1} (bin width $dr = 30.25 \mu\text{m}$). Agreement is poor in the low-wind conditions (Figs. 14a–c) because wind stress and wave heights are insufficient to entrain many bubbles, impacting the brightness gradients and foreground–background separation involved in the bubble identification process. Our parameterization thus carries with it the expectation that increased input from wind to waves per unit significant wave height results in a broadening

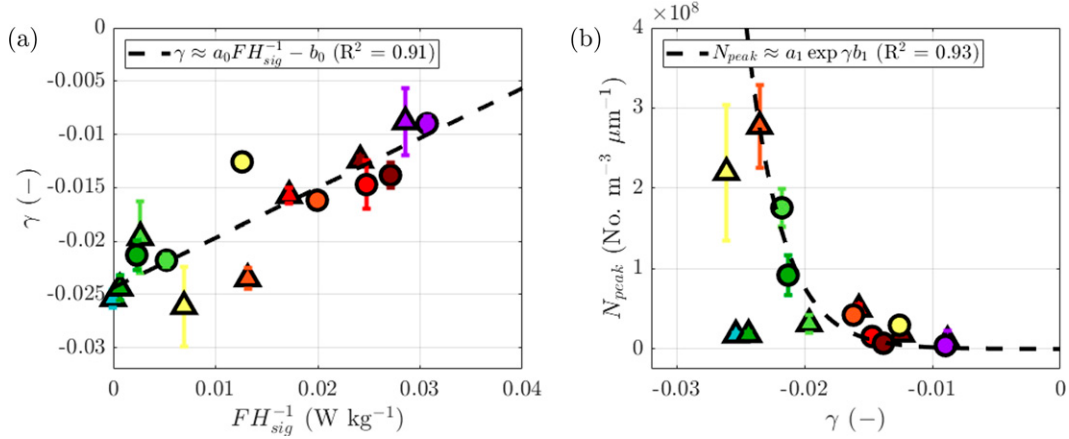


FIG. 13. Exponential distribution parameters and their relationship to wave-scaled wind input to waves FH_{sig}^{-1} . (a) Bubble radius decay rate γ and (b) number of bubbles at the distribution peak N_{peak} determined via γ . Colors indicate the 10-m equivalent wind speed U_{10} , and as previously, circles and triangles represent data from monochromatic and JONSWAP spectrum wave conditions, respectively.

of the distributions resulting in less bubbles at the peak radius and a slower decay rate. In a similar way, the bubble size distributions from beneath monochromatic wave conditions and their parameterized fits are shown in Fig. 15.

As in the JONSWAP wave spectrum experiments, bubble size distributions show broadening and decrease in average bubble size from $r = 166 \mu\text{m}$ to $r = 45 \mu\text{m}$ as wind forcing increases, generally from $U_{10} \geq 27.2$. Using the parameters from the exact fits, N_{peak} takes a maximum in both wave

conditions for $U_{10} = 27.2\text{--}36.3 \text{ m s}^{-1}$, decreasing thereafter as the bubble size distributions broaden to include other bubble radii. Similarly, γ takes its most negative values in that wind speed range and then begins to increase toward zero such that the rate of bubble loss at higher radius is less rapid. Since wave breaking and the turbulent kinetic energy flux associated with it are integral to the production and separation of bubbles across a variety of radii, in the next subsection we complete the connection between sea

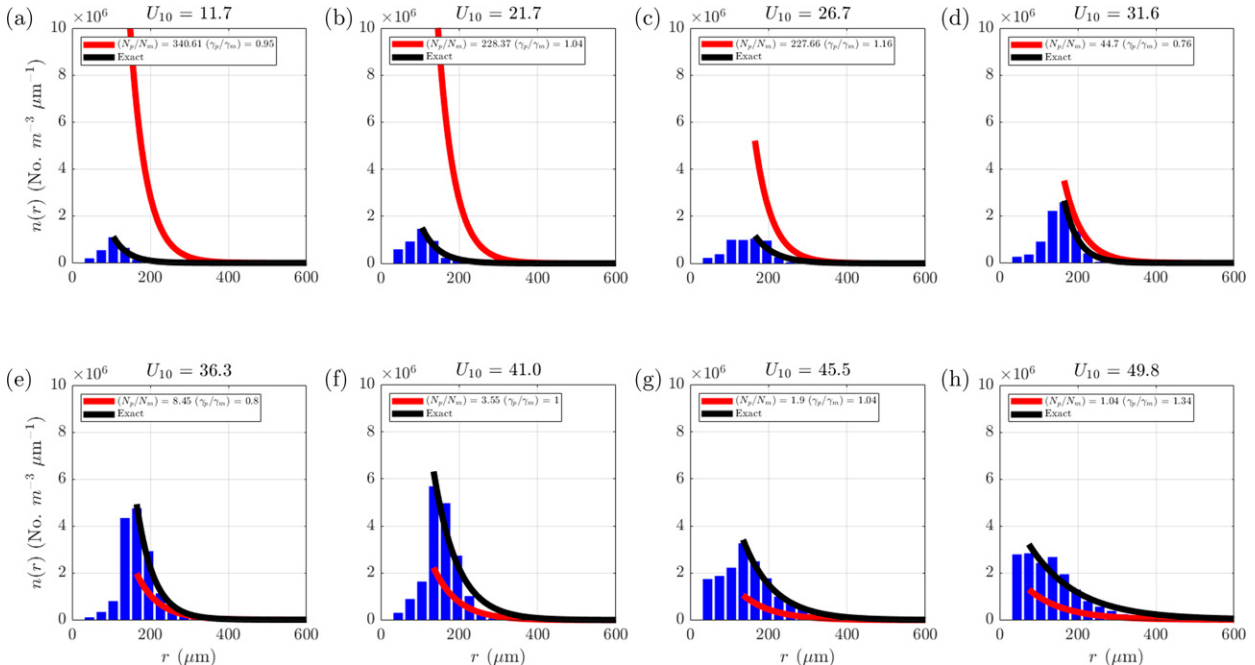


FIG. 14. (a)–(h) Observed and parameterized bubble size distributions in the JONSWAP spectrum wave conditions. Histograms depicting the observed distributions are in blue bars, the parameterized distribution is plotted in red. The exact fits are given in black. The ratio of parameterized and observed distribution parameters as previously described are given in each panel. The title indicates the wind speed in each panel.

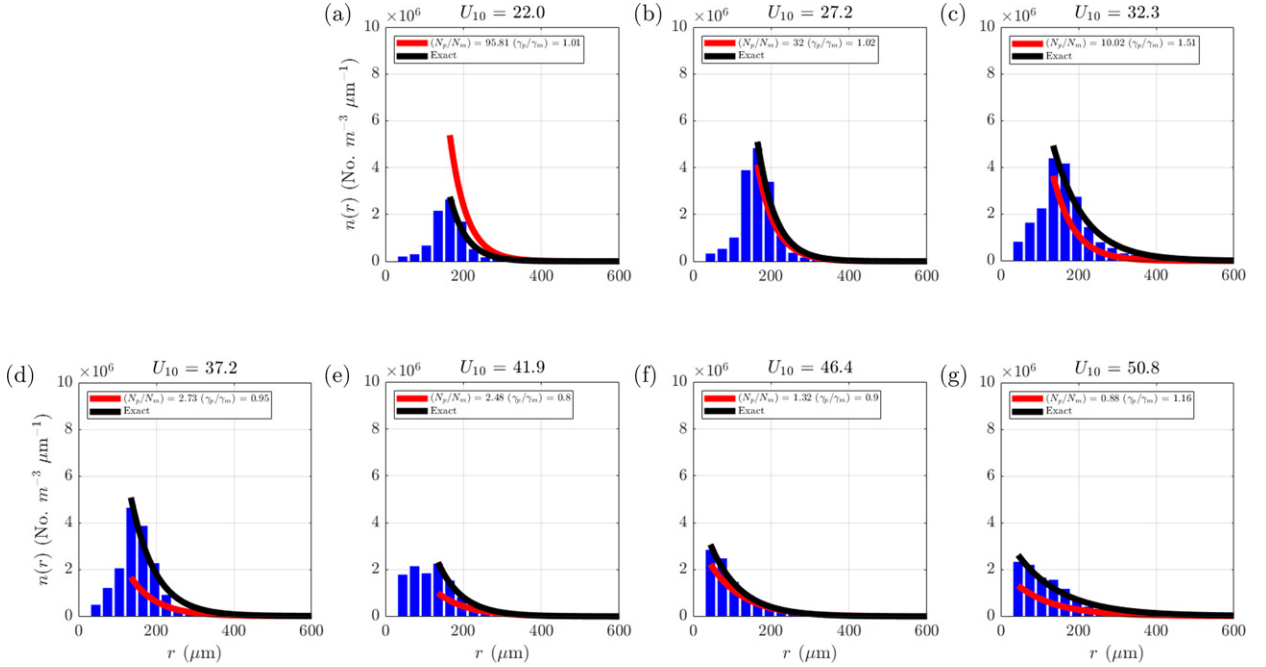


FIG. 15. (a)–(g) Observed and parameterized bubble size distributions in the monochromatic wave conditions. Histograms depicting the observed distributions are in blue bars, the parameterized distribution is plotted in red. The exact fits are again given in black. The ratios of distribution parameters are also given. The title indicates the wind speed in each panel.

surface structure and subsurface turbulence using surface wave and subsurface ADCP turbulence measurements.

e. Subsurface turbulent kinetic energy and dissipation

Here, we use our laboratory measurements of subsurface turbulence and dissipation beneath different wind-wave environments to extend previous data to the hurricane-force wind-wave regime. Wave scaling of dissipation rate follows the method used on fixed tower measurements by Terray et al. (1996) at the Canada Centre for Inland Waters (CCIW), and by Drennan et al. (1996) based on underway vessel data from the R/V *Frederick G. Creed*. The wave-scaled dissipation rate $\epsilon H_{\text{sig}} F^{-1}$ includes significant wave height as multiplier to the raw measurement, while the wind-to-wave energy input F reduces the wave-scaling effects as more energy input occurs from wind to waves.

In Fig. 16, we show the midprofile zonal velocity spectrum $S_{uu}(f)$ for both wave types with increasing 10-m equivalent wind speed U_{10N} . In the JONSWAP wave spectrum experiments (blue curves), spectra were flat or nearly flat at frequencies lower than the expected peak near $f \approx 1.00$ Hz. Wave band development can be seen progressively from Figs. 16c to 16h, with the peak frequency shifting from $f_p = 4.30$ Hz to $f_p = 0.93$ Hz with wind speed increasing with each panel. The inertial subrange slope in the velocity spectra where $U_{10N} \geq 34$ m s⁻¹ (hurricane force) are -2.05 , -1.73 , -1.67 , and -1.67 , respectively. At wind speeds less than this, the portion of the turbulence spectra determined to be isotropic (via ARIIS, see section 3d) includes wave band energy contributions. Comparing to the monochromatic wave experiments (red), again, at lower wind

speeds the wave band may be part of the identified inertial subrange. At wind speeds $U_{10N} \geq 27$ m s⁻¹, the wave band is broader with less spectral density, while it narrows considerably to the frequency range expected of prescribed monochromatic waves at moderate and high winds. Additionally, the average area beneath the inertial subrange of the spectra indicates the turbulent kinetic energy to be $5.65 \times 10^{-4} \pm 6.4 \times 10^{-4}$ m² s⁻² beneath high-wind ($U_{10N} \geq 34$ m s⁻¹) JONSWAP spectrum waves and $1.01 \times 10^{-3} \pm 6.2 \times 10^{-4}$ m² s⁻² under similar monochromatic wave conditions—a difference of 76.9%. Based on this, we expect larger TKE dissipation rates beneath monochromatic waves, where the isotropic turbulence in the inertial subrange extends to higher frequencies than those in JONSWAP spectrum wave conditions.

From the subsurface velocity spectra, expected slope above the peak frequency and subsequent energy spectral density do not conform to the $f^{-5/3}$ values over much of the spectrum in low-wind conditions where wave breaking is infrequent, or occurring at scales insufficient to produce sufficient scatterers below the air-water interface (i.e., Figs. 16a–d). Given manufacturer guidelines, the Nortek Vectrino II 3D ADCP is effective at resolving turbulence where signal-to-noise ratio (SNR) is greater than 20 dB throughout the profile. In Fig. 17, we quantify the relationship between wave-scaled wind-wave energy input FH_{sig}^{-1} and both SNR and subsurface TKE dissipation rate $\bar{\epsilon}$. TKE dissipation rates spanned the range $\bar{\epsilon}_S = 2.7 \times 10^{-3} - 1.2 \times 10^{-2}$ m² s⁻³ beneath JONSWAP spectrum waves and $\bar{\epsilon}_M = 4.7 \times 10^{-3} - 1.3 \times 10^{-2}$ m² s⁻³ beneath monochromatic waves, respectively. In Fig. 17a, SNR is observed to be larger beneath monochromatic waves and to

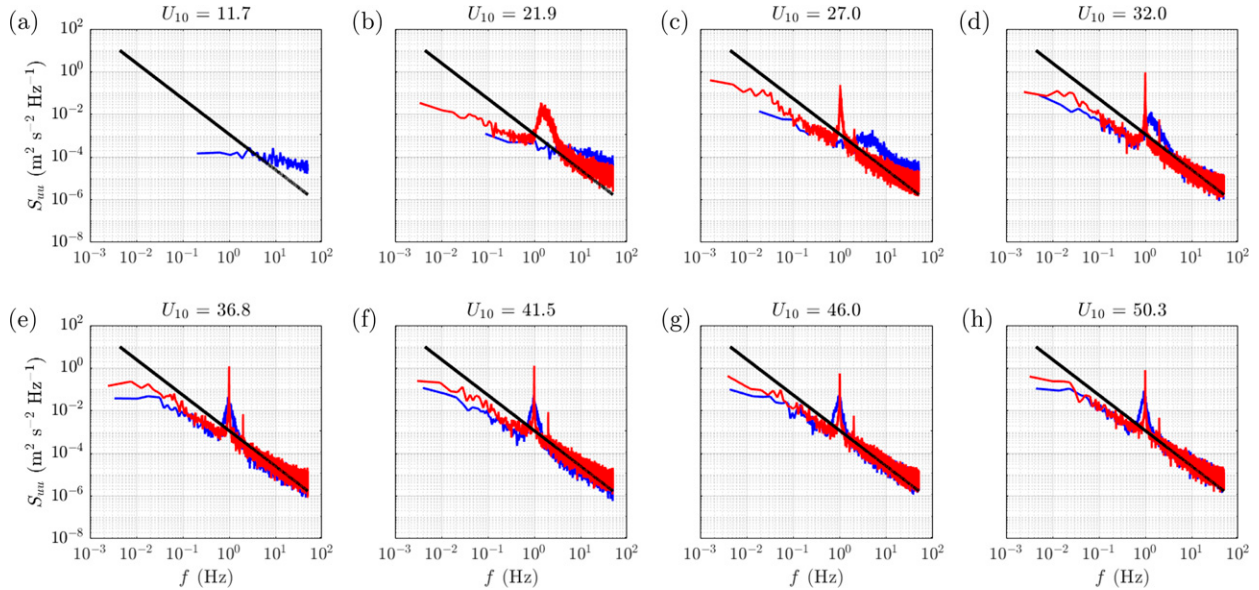


FIG. 16. Vectrino II 3D ADCP derived zonal water velocity spectra $S_{uu}(f)$ beneath JONSWAP wave spectrum (blue) and monochromatic (red) waves subject to the indicated wind speed U_{10} . The solid black line in each panel is $f^{-5/3}$.

increase with FH_{sig}^{-1} , indicating a larger signal and more scatterers present. Where the ADCP SNR is sufficient, dissipation rates $\bar{\epsilon}$ in Fig. 17b increase with FH_{sig}^{-1} following the linear fit $\bar{\epsilon} \approx 0.42FH_{sig}^{-1}$ with $R^2 = 0.99$.

f. Bubble-turbulence interactions

In prior literature from field studies (e.g., Blanchard and Woodcock 1957; Medwin 1970; Johnson and Cooke 1979) and laboratory experiments (e.g., Koga 1982; Hwang et al. 1991; Deane and Stokes 2002), acoustic and optical techniques have been used to capture bubbles and connect the observed size

distributions to surface wave conditions or subsurface velocity and turbulence measurements. Here, we extend that effort in reporting the linkage between subsurface turbulent kinetic energy dissipation and bubble size distributions beneath an air-water interface composed of wind-wave conditions up to hurricane force. We do this by presenting relationships between the wave-scaled wind input FH_{sig}^{-1} , the average subsurface TKE dissipation rate $\bar{\epsilon}$, and the observed void fraction of the bubble plumes α_b .

Derived from independent instruments, Fig. 18 shows the subsurface ADCP-derived TKE dissipation rates and shadowgraph

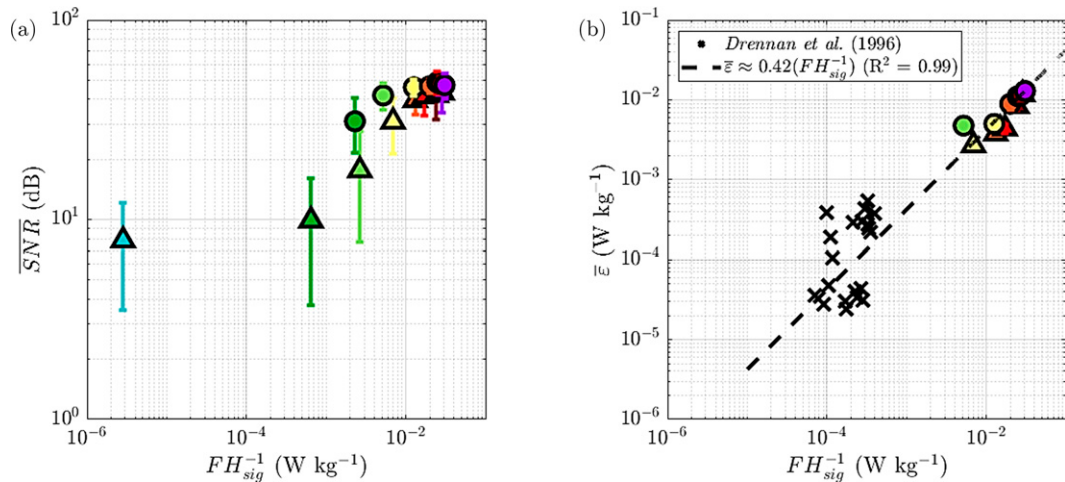


FIG. 17. (a) Signal-to-noise ratio and (b) TKE dissipation rate averaged over the center of the Vectrino II 3D ADCP profile. Colors corresponding to U_{10} and wave conditions indicated as JONSWAP (with triangles) or monochromatic (with circles) as before. Dissipation rates derived from zonal subsurface velocity spectra in Drennan et al. (1996) are shown in black crosses in (b). Error bars are one standard deviation.

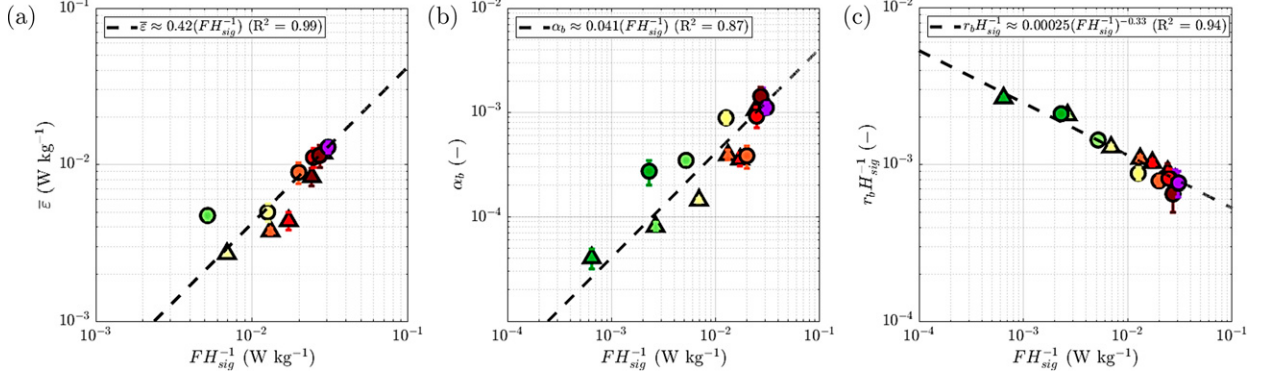


FIG. 18. (a) TKE dissipation rate averaged over the center of the Vectrino II 3D ADCP profile and (b) void fraction calculated from the shadowgraph image-derived bubble size distributions, and (c) average bubble radius scaled by significant wave height, as functions of the wave-scaled rate of energy input from the wind to waves, FH_{sig}^{-1} . Colors corresponding to U_{10} and wave conditions indicated as JONSWAP (with triangles) or monochromatic (with circles) as before. Error bars are one standard deviation.

image-derived void fractions as a function of FH_{sig}^{-1} . As momentum flux from the wind to the surface wave field results in wave growth proportional to the alignment of wind and waves (e.g., short-crested JONSWAP spectrum versus the long-crested monochromatic waves), a combination of visible micro-breaking between wave crests and white-capping resulted in greater void fractions captured in the images taken from the shadowgraph. At the lower wind speeds, this is particularly true for the monochromatic waves as Fig. 12 shows the greater wind-wave energy flux (via breaking) and the degree to which bubbles are distinguished from the background volume. Furthermore, TKE dissipation rates also increase with FH_{sig}^{-1} as more frequent and intense wave breaking results in an increase in shear turbulence. Scaling the average bubble radius with significant wave height, Fig. 18c

demonstrates that in the context of a greater volume of bubbles with more turbulent kinetic energy present as FH_{sig}^{-1} increases, the importance of wave growth and breaking to the size of bubbles in the distributions increases as well. At low wind speeds, the average bubble radius increases for a time where H_{sig} is small and white-capping is less frequent. As wind input and wave heights increase, the increased prevalence of wave breaking in moderate and high winds results in greater subsurface turbulence, pressure compression of bubbles and a reduction in average bubble radius.

Finally, we examine the wave-scaled TKE dissipation rates and bubble void fraction together using wave-scaled depth coordinates of Terray et al. (1996), zH_{sig}^{-1} (Fig. 19). Our data lie along the power law fit with Surface Waves Dynamics Experiments (SWADE) and Water Air Vertical Exchange Studies

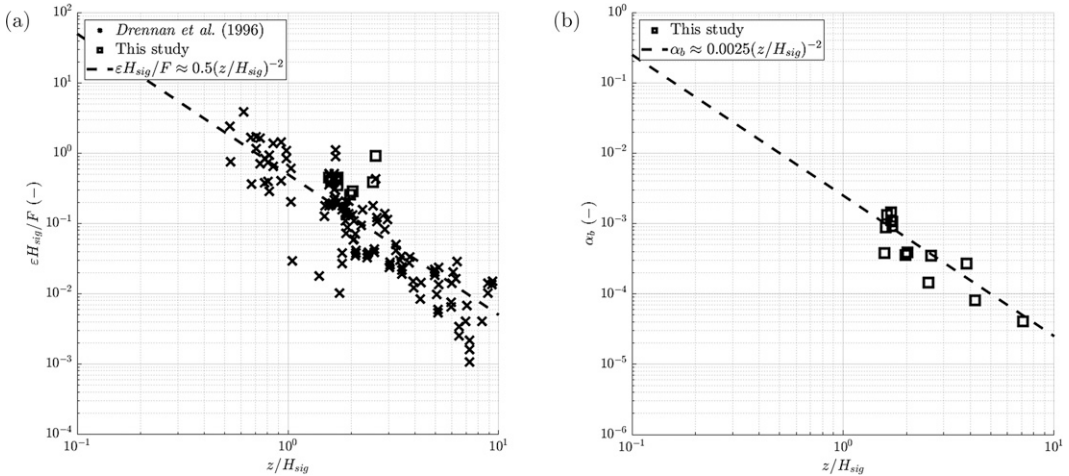


FIG. 19. (a) Wind-input scaled TKE dissipation rate and (b) bubble void fraction vs wave-scaled depth using the coordinates from Terray et al. (1996). Included in crosses are the data from SWADE and WAVES field experiments, reported in Drennan et al. (1996) and Terray et al. (1996), respectively. Our data are given by the squares. The dashed line is a best fit of the data with the form $\varepsilon H_{sig}/F \approx 0.5(z/H_{sig})^{-2}$ shifted in amplitude to reflect the full dataset plotted here but based on the power-law fit in Drennan et al. (1996, their Fig. 5). In (b), the dashed line gives a best fit to the α_b data using a similar functional form to that in (a).

(WAVES) values supporting the wave-dependent scaling as valid in our laboratory or the field data. Our significant wave heights were 0.02–0.19 m, where in SWADE and WAVES they were 0.90–2.60 m and 0.20–0.30 m, respectively. With greater significant wave heights in the surface wave field there is greater turbulence dissipation per wind input FH_{sig}^{-1} at shallower depths nearer to the surface. In a similar vein, the air or void fraction of bubbles we observed increases with decreasing wave-scaled depth. Given our essentially fixed depth measurement of these bubbles ($z \approx 0.30$ m), the increase in α_b is in response to greater significant wave heights and the subsequent breaking-induced volume fluxes of air.

5. Conclusions

Laboratory experiments designed to investigate bubble dynamics and air-sea gas transfer at high winds provided data for directly connecting wave structure and wave breaking in up to hurricane-force winds to the production of bubbles, subsurface turbulence, and its dissipation. Laboratory waves modeled after the JONSWAP wave spectrum (Hasselmann et al. 1973) produced gradually increasing wave spectra, decreasing wave frequency and wavenumber with increasing wind stress. Wave breaking was found to occur more frequently and with greater intensity in the steeper monochromatic wave conditions, and the breaking prevalence increases most rapidly between $U_{10} = 27$ and 37 m s^{-1} .

Bubble size distributions from field, numerical, and laboratory studies including this study can be parameterized using an exponential distribution from and above their distribution peak radius. This distribution is reasonable for bubbles observed in actively breaking wave crests and more diffuse plumes. Bubble statistics including void fraction, number, and radius of bubbles were each expressed in terms of the energy input from wind to the waves, FH_{sig}^{-1} . Increasing wind stress and wave height were found to result in greater air volume entrainment and a greater number of bubbles. Air entrainment is greater in the more frequently and intensely breaking monochromatic wave conditions. Bubble size, however, decreases with FH_{sig}^{-1} . Large bubbles buoyantly de-gas or are fragmented by subsurface turbulent shear instigated by the wave breaking events. Subsurface images show bubbles move freely and separately at low FH_{sig}^{-1} , but become occasionally and then extensively clustered in the most turbulent conditions. Using exponential distribution parameterization, bubble size distributions become broader and more negatively skewed with increasing surface roughness and breaking waves of greater height.

Wind-wave energy input determined using wave growth rate and directional wave spectra was found to be larger in monochromatic wave conditions. Significant wave height and directional spectra demonstrate a more narrow-banded wave field and larger growth rate are present with these monochromatic waves. Subsurface velocity, stress, and ADCP SNR are each larger in monochromatic than JONSWAP spectrum wave conditions, owing to the increased probability and intensity of wave breaking. SNR is found to be weak in low-wind conditions, particularly for JONSWAP spectrum waves, as a

direct consequence of the smaller wave heights and less vigorous breaking events resulting in fewer subsurface scatterers (e.g., bubbles).

Wave-scaled TKE dissipation rates in laboratory and field data from SWADE (Drennan et al. 1996) and WAVES (Terray et al. 1996) follow power law fits with wave-scaled depth. Wave-scaled dissipation rates are larger in monochromatic wave conditions and increase toward smaller wave-scaled depth. With increasing wind stress, wave breaking, and subsurface turbulence, fewer large bubbles remain either due to buoyant outgassing, horizontal advection, or fragmentation due to shear turbulence. A greater number of small bubbles is observed, particularly in monochromatic wave conditions, and the bubble distribution slope at high radii decreases as a result.

Our results demonstrate that evolution and breaking of the sea surface wave field results in diverse bubble populations even observable at hurricane-force conditions, the distributions of which can be linked to the energy flux from the wind to sea surface waves. Furthermore, increased breaking probability and intensity of the steeper monochromatic laboratory waves results in a greater number of small bubbles and enhanced subsurface shear turbulence induced by the wave-breaking events. Subsurface imaging of bubbles has also demonstrated interaction between bubbles through clustering actively occurs, particularly at high winds where whitecaps and breaking can be seen.

Although our laboratory measurements are constrained in water depth, fetch, and in the scale of waves (e.g., significant wave height) relative to the open ocean, the physical mechanisms involved in air entrainment and bubble production via breaking waves have been shown to be quite scale-independent (Carey et al. 1993; Su and Cartmill 1995; Krall et al. 2019). These studies have involved tipping buckets and wind-wave flumes with volumes from 276 to 1107 m^3 ; however, we still observe key forces and physics relevant to air-sea gas exchange such as wave-orbital motions, jet intrusions, air cavity collapse, bubble rise, cohesion, and filaments (Deane and Stokes 1999; Deane and Stokes 2002; Krall et al. 2019). Despite this, bubble motion, lifetime, and potential gas exchange to the ocean may be missing in depth-limited laboratory tanks, necessitating the need for vertical scaling and full-depth ADCP profiles and bubble imaging to ascertain the full picture.

Furthermore, although our mechanically generated paddle waves physically behave like swell, swell has been observed to dominate the wave spectrum in hurricanes (Whalen and Ochi 1978; Ochi and Chiu 1982; Young 1997), with wind sea seen above about 3 times the peak frequency, $3f_p$ (Young and Babanin 2006). Such one-dimensional wave spectra have been parameterized using the generalized JONSWAP spectrum form proposed in Donelan et al. (1985). As such, the wind-wave conditions in the present study, which feature swell-like waves subject to hurricane-force winds are likely appropriate for comparison with open ocean observations. Future experiments implementing NDBC buoy observed wave spectra in the SUSTAIN wind-wave tank could provide a useful, more realistic wave state and bubble size distributions that further elucidate air-sea gas exchange in

extreme wind conditions. Additional future research using purely wind generated waves and imaging bubbles in actively breaking wave crests, combined with full-depth profiles of subsurface turbulence for the computation of shear and dissipation are also recommended to more fully understand and parameterize air-sea exchanges governed by waves and their breaking.

Acknowledgments. We gratefully acknowledge the assistance of the entire Alfred C. Glassell Jr. SUSTAIN laboratory at the University of Miami in executing the experiments and collecting the raw physical data, and Wellesley College students Helene Alt, Danielle Aldrett, Emily Kopp, and Lumi Kinjo for collecting the noble gas data. We extend special thanks to Cedric Guigand for his assistance in setup and installation of the bubble imager. This work was supported by Grant OCE1634432 and Grant OCE1634467 from the National Science Foundation (NSF).

Data availability statement. Data are publicly available through the Biological and Chemical Oceanography Data Management Office (BCO-DMO) at <https://www.bco-dmo.org/project/776111>.

REFERENCES

- Atherton, T. J., and D. J. Kerbyson, 1993: The coherent circle Hough transform. *Proc. 4th British Machine Vision Conf.*, Surrey, United Kingdom, British Machine Vision Association, 269–278, <https://doi.org/10.5244/C.7.27>.
- , and —, 1999: Size invariant circle detection. *Image Vis. Comput.*, **17**, 795–803, [https://doi.org/10.1016/S0262-8856\(98\)00160-7](https://doi.org/10.1016/S0262-8856(98)00160-7).
- Babanin, A., D. Chalikov, I. Young, and I. Savelyev, 2007: Predicting the breaking onset of surface water waves. *Geophys. Res. Lett.*, **34**, L07605, <https://doi.org/10.1029/2006GL029135>.
- Banner, M. L., X. Barthelemy, F. Fedele, M. Allis, A. Benetazzo, F. Dias, and W. L. Peirson, 2014: Linking reduced breaking crest speeds to unsteady nonlinear water wave group behavior. *Phys. Rev. Lett.*, **112**, 114502, <https://doi.org/10.1103/PhysRevLett.112.114502>.
- Benilov, A., and B. Filyushkin, 1970: Application of methods of linear filtration to an analysis of fluctuations in the surface layer of the sea. *Izv., Atmos. Ocean. Phys.*, **6**, 810–819.
- Blanchard, D., and A. Woodcock, 1957: Bubble formation and modification in the sea and its meteorological Significance. *Tellus*, **9**, 145–158, <https://doi.org/10.3402/tellusa.v9i2.9094>.
- Bricker, J. D., and S. G. Monismith, 2007: Spectral wave-turbulence decomposition. *J. Atmos. Oceanic Technol.*, **24**, 1479–1487, <https://doi.org/10.1175/JTECH2066.1>.
- Brumer, S. E., C. J. Zappa, B. W. Blomquist, C. W. Fairall, A. Cifuentes-Lorenzen, J. B. Edson, I. M. Brooks, and B. J. Huebert, 2017: Wave-related Reynolds number parameterizations of CO₂and DMS transfer velocities. *Geophys. Res. Lett.*, **44**, 9865–9875, <https://doi.org/10.1002/2017GL074979>.
- Buckley, M. P., and F. Veron, 2017: Airflow measurements at a wavy air-water interface using PIV and LIF. *Exp. Fluids*, **58**, 161, <https://doi.org/10.1007/s00348-017-2439-2>.
- Callaghan, A. H., M. D. Stokes, and G. B. Deane, 2014: The effect of water temperature on air entrainment, bubble plumes, and surface foam in a laboratory breaking-wave analog. *J. Geophys. Res. Oceans*, **119**, 7463–7482, <https://doi.org/10.1002/2014JC010351>.
- Carey, W., J. W. Fitzgerald, E. C. Monahan, and Q. Wang, 1993: Measurement of the sound produced by a tipping trough with fresh and salt water. *J. Acoust. Soc. Amer.*, **93**, 3178–3192, <https://doi.org/10.1121/1.405702>.
- Cassar, N., B. A. Barnett, M. L. Bender, J. Kaiser, R. C. Hamme, and B. Tilbrook, 2009: Continuous high-frequency dissolved O₂/Ar measurements by equilibrator inlet mass spectrometry. *Anal. Chem.*, **81**, 1855–1864, <https://doi.org/10.1021/ac802300u>.
- Caulliez, G., 2002: Self-similarity of near-breaking short gravity wind waves. *Phys. Fluids*, **14**, 2917–2920, <https://doi.org/10.1063/1.1487380>.
- Curcic, M., and B. K. Haus, 2020: Revised estimates of ocean surface drag in strong winds. *Geophys. Res. Lett.*, **47**, e2020GL087647, <https://doi.org/10.1029/2020GL087647>.
- Deane, G. B., 1997: Sound generation and air entrainment by breaking waves in the surf zone. *J. Acoust. Soc. Amer.*, **102**, 2671–2689, <https://doi.org/10.1121/1.420321>.
- , and M. D. Stokes, 1999: Air entrainment processes and bubble size distributions in the surf zone. *J. Phys. Oceanogr.*, **29**, 1393–1403, [https://doi.org/10.1175/1520-0485\(1999\)029<1393:aepabs>2.0.co;2](https://doi.org/10.1175/1520-0485(1999)029<1393:aepabs>2.0.co;2).
- , and —, 2002: Scale dependence of bubble creation mechanisms in breaking waves. *Nature*, **418**, 839–844, <https://doi.org/10.1038/nature00967>.
- , —, and A. H. Callaghan, 2016: The saturation of fluid turbulence in breaking laboratory waves and implications for whitecaps. *J. Phys. Oceanogr.*, **46**, 975–992, <https://doi.org/10.1175/JPO-D-14-0187.1>.
- Dempster, A. P., N. M. Laird, and D. B. Rubin, 1977: Maximum likelihood from incomplete data via the EM algorithm. *J. Roy. Stat. Soc.*, **B39**, 1–22, <https://doi.org/10.1111/j.2517-6161.1977.tb01600.x>.
- Donelan, M. A., J. Hamilton, and W. Hui, 1985: Directional spectra of wind-generated waves. *Philos. Trans. Roy. Soc.*, **A315**, 509–562, <https://doi.org/10.1098/rsta.1985.0054>.
- , W. M. Drennan, and A. K. Magnusson, 1996: Nonstationary analysis of the directional properties of propagating waves. *J. Phys. Oceanogr.*, **26**, 1901–1914, [https://doi.org/10.1175/1520-0485\(1996\)026<1901:NAOTDP>2.0.CO;2](https://doi.org/10.1175/1520-0485(1996)026<1901:NAOTDP>2.0.CO;2).
- , B. K. Haus, N. Reul, W. J. Plant, M. Stiassnie, H. C. Gruber, O. B. Brown, and E. S. Saltzman, 2004: On the limiting aerodynamic roughness of the ocean in very strong winds. *Geophys. Res. Lett.*, **31**, L18306, <https://doi.org/10.1029/2004GL019460>.
- Drennan, W. M., M. A. Donelan, E. A. Terray, and K. B. Katsaros, 1996: Oceanic turbulence dissipation measurements in SWADE. *J. Phys. Oceanogr.*, **26**, 808–815, [https://doi.org/10.1175/1520-0485\(1996\)026<0808:OTDMIS>2.0.CO;2](https://doi.org/10.1175/1520-0485(1996)026<0808:OTDMIS>2.0.CO;2).
- Edson, J. B., and Coauthors, 2013: On the exchange of momentum over the open ocean. *J. Phys. Oceanogr.*, **43**, 1589–1610, <https://doi.org/10.1175/JPO-D-12-0173.1>.
- Elsayed, M. A., 2008: Application of continuous wavelet analysis in distinguishing breaking and nonbreaking waves in the wind-wave time series. *J. Coastal Res.*, **24**, 273–277, <https://doi.org/10.2112/05-0443.1>.
- Fairall, C. W., and S. E. Larsen, 1986: Inertial-dissipation methods and turbulent fluxes at the air-ocean interface. *Bound.-Layer Meteor.*, **34**, 287–301, <https://doi.org/10.1007/BF00122383>.
- Gemmrich, J. R., 2010: Breaking waves and near-surface turbulence. *Encyclopedia of Ocean Sciences*, Elsevier, 431–438, <https://doi.org/10.1016/B978-012374473-9.00641-X>.

- , and D. M. Farmer, 2004: Near-surface turbulence in the presence of breaking waves. *J. Phys. Oceanogr.*, **34**, 1067–1086, [https://doi.org/10.1175/1520-0485\(2004\)034<1067:NTITPO>2.0.CO;2](https://doi.org/10.1175/1520-0485(2004)034<1067:NTITPO>2.0.CO;2).
- Goring, D., and V. Nikora, 2002: Despiking acoustic Doppler velocimeter data. *J. Hydraul. Eng.*, **128**, 117–126, [https://doi.org/10.1061/\(ASCE\)0733-9429\(2002\)128:1\(117\)](https://doi.org/10.1061/(ASCE)0733-9429(2002)128:1(117)).
- Hara, T., and P. P. Sullivan, 2015: Wave boundary layer turbulence over surface waves in a strongly forced condition. *J. Phys. Oceanogr.*, **45**, 868–883, <https://doi.org/10.1175/JPO-D-14-0116.1>.
- Hasselmann, K., and Coauthors, 1973: Measurements of wind-wave growth and swell decay during the joint North Sea wave project (JONSWAP). *Dtsch. Hydrogr. Z.*, **8** (12), 1–95.
- Hinze, J. O., 1955: Fundamentals of the hydrodynamic mechanism of splitting in dispersion processes. *AIChE J.*, **1**, 289–295, <https://doi.org/10.1002/aic.690010303>.
- Holthuijsen, L. H., and T. H. C. Herbers, 1986: Statistics of breaking waves observed as whitecaps in the open sea. *J. Phys. Oceanogr.*, **16**, 290–297, [https://doi.org/10.1175/1520-0485\(1986\)016<0290:SOBWOA>2.0.CO;2](https://doi.org/10.1175/1520-0485(1986)016<0290:SOBWOA>2.0.CO;2).
- Huang, N. E., S. R. Long, M. A. Donelan, Y. Yuan, and J. Lai, 1992: The local properties of ocean surface waves by the phase-time method. *Geophys. Res. Lett.*, **19**, 685–688, <https://doi.org/10.1029/92GL00670>.
- Hwang, P. A., D. Xu, and J. Wu, 1989: Breaking of wind-generated waves: Measurements and characteristics. *J. Fluid Mech.*, **202**, 177–200, <https://doi.org/10.1017/S002211208900114X>.
- , Y.-K. Poon, and J. Wu, 1991: Temperature effects on generation and entrainment of bubbles induced by a water jet. *J. Phys. Oceanogr.*, **21**, 1602–1605, [https://doi.org/10.1175/1520-0485\(1991\)021<1602:TEOGAE>2.0.CO;2](https://doi.org/10.1175/1520-0485(1991)021<1602:TEOGAE>2.0.CO;2).
- Jeffreys, H., 1924: On the formation of waves by wind. *Proc. Roy. Soc., A*, **107**, 189–206, <https://doi.org/10.1098/rspa.1925.0015>.
- , 1925: On the formation of waves by wind, II. *Proc. Roy. Soc., A*, **110**, 341–347, <https://doi.org/10.1098/rspa.1926.0014>.
- Jimenez, J., A. A. Wray, P. G. Saffman, and R. S. Rogallo, 1993: The structure of intense vorticity in isotropic turbulence. *J. Fluid Mech.*, **255**, 65–90, <https://doi.org/10.1017/S0022112093002393>.
- Johnson, B. D., and R. C. Cooke, 1979: Bubble populations and spectra in coastal waters: A photographic approach. *J. Geophys. Res.*, **84**, 3761, <https://doi.org/10.1029/JC084iC07p03761>.
- Kinjo, L., 2019: Quantifying air-sea gas exchange at high wind speeds using noble gas measurements: Insights from the SUSTAIN wind-wave tank. Honors thesis, Dept. of Chemistry, Wellesley College, 8 pp., <https://repository.wellesley.edu/object/ir901>.
- Kinsman, B., 1965: *Wind Waves, Their Generation and Propagation on the Ocean Surface*. Prentice Hall, 676 pp.
- Koga, M., 1982: Bubble entrainment in breaking wind waves. *Tellus*, **34**, 481–489, <https://doi.org/10.3402/tellusa.v34i5.10833>.
- Kolmogorov, A. N., 1941: The local structure of turbulence in incompressible viscous fluid for very large Reynolds numbers. *Proc. Roy. Soc. London, A*, **434**, 9–13, <https://doi.org/10.1098/rspa.1991.0075>.
- Krall, K. E., A. W. Smith, N. Takagaki, and B. Jaehne, 2019: Air-sea gas exchange at wind speeds up to 85 m s^{-1} . *Ocean Sci.*, **15**, 1783–1799, <https://doi.org/10.5194/os-15-1783-2019>.
- Large, W. G., and S. Pond, 1981: Open ocean momentum flux measurements in moderate to strong winds. *J. Phys. Oceanogr.*, **11**, 324–336, [https://doi.org/10.1175/1520-0485\(1981\)011<0324:OOMFMI>2.0.CO;2](https://doi.org/10.1175/1520-0485(1981)011<0324:OOMFMI>2.0.CO;2).
- Larson, T., and J. Wright, 1975: Wind-generated gravity-capillary waves: Laboratory measurements of temporal growth rates using microwave backscatter. *J. Fluid Mech.*, **97**, 455–479, <https://doi.org/10.1017/S002211207500211X>.
- Laxague, N. J., B. K. Haus, D. G. Ortiz-Suslow, C. J. Smith, G. Novelli, H. Dai, T. Özgökmen, and H. C. Graber, 2017: Passive optical sensing of the near-surface wind-driven current profile. *J. Atmos. Oceanic Technol.*, **34**, 1097–1111, <https://doi.org/10.1175/JTECH-D-16-0090.1>.
- Liberzon, D., A. Vreme, S. Knobler, and I. Bentwich, 2019: Detection of breaking waves in single wave gauge records of surface elevation fluctuations. *J. Atmos. Oceanic Technol.*, **36**, 1863–1879, <https://doi.org/10.1175/JTECH-D-19-0011.1>.
- Liu, P., 1993: Estimating breaking wave statistics from wind-wave time series data. *Ann. Geophys.*, **11**, 970–972.
- Lumley, J. L., and E. A. Terray, 1983: Kinematics of turbulence convected by a random wave field. *J. Phys. Oceanogr.*, **13**, 2000–2007, [https://doi.org/10.1175/1520-0485\(1983\)013<2000:KOTCBA>2.0.CO;2](https://doi.org/10.1175/1520-0485(1983)013<2000:KOTCBA>2.0.CO;2).
- Manning, C. C., R. H. Stanley, and D. E. Lott, 2016: Continuous measurements of dissolved Ne, Ar, Kr, and Xe ratios with a field-deployable gas equilibration mass spectrometer. *Anal. Chem.*, **88**, 3040–3048, <https://doi.org/10.1021/acs.analchem.5b03102>.
- Marple, S. L., 1999: Computing the discrete-time “analytic” signal via FFT. *IEEE Trans. Sig. Proc.*, **47**, 2849, <https://doi.org/10.1109/78.782222>.
- Medwin, H., 1970: In situ acoustic measurements of bubble populations in coastal ocean waters. *J. Geophys. Res.*, **75**, 599–611, <https://doi.org/10.1029/JC075i003p00599>.
- , 1977: In situ acoustic measurements of microbubbles at sea. *J. Geophys. Res.*, **82**, 971–976, <https://doi.org/10.1029/JC082i006p00971>.
- Ochi, M., and M. Chiu, 1982: Nearshore wave spectra measured during Hurricane David. *Coastal Eng. Proc.*, **1**, 5, <https://doi.org/10.9753/icce.v18.5>.
- Oppenheim, A. V., R. W. Schafer, and J. R. Buck, 1999: *Discrete-Time Signal Processing*. 2nd ed. Prentice Hall, 870 pp.
- Ortiz-Suslow, D. G., and Q. Wang, 2019: An evaluation of Kolmogorov’s $-5/3$ power law observed within the turbulent airflow above the ocean. *Geophys. Res. Lett.*, **46**, 14 901–14 911, <https://doi.org/10.1029/2019GL085083>.
- , —, J. Kalogiros, and R. Yamaguchi, 2020: A method for identifying Kolmogorov’s inertial subrange in the velocity variance spectrum. *J. Atmos. Oceanic Technol.*, **37**, 85–102, <https://doi.org/10.1175/JTECH-D-19-0028.1>.
- Özgökmen, T. M., and Coauthors, 2018: Technological advances for ocean surface measurements by the consortium for advanced research on transport of hydrocarbons in the environment (CARTHE). *Mar. Technol. Soc. J.*, **52**, 71–76, <https://doi.org/10.4031/MTSJ.52.6.11>.
- Plant, W. J., W. C. Keller, V. Hesany, T. Kara, E. Bock, and M. A. Donelan, 1999: Bound waves and Bragg scattering in a wind-wave tank. *J. Geophys. Res.*, **104**, 3243–3263, <https://doi.org/10.1029/1998JC00061>.
- , P. H. Dahl, J. P. Giovanangeli, and H. Branger, 2004: Bound and free surface waves in a large wind-wave tank. *J. Geophys. Res.*, **109**, C10002, <https://doi.org/10.1029/2004JC002342>.
- Rapp, R. J., and W. K. Melville, 1990: Laboratory measurements of deep-water breaking waves. *Philos. Trans. Roy. Soc., A*, **331**, 735–800, <https://doi.org/10.1098/rsta.1990.0098>.

- Rensen, J., S. Luther, and D. Lohse, 2005: The effect of bubbles on developed turbulence. *J. Fluid Mech.*, **538**, 153–187, <https://doi.org/10.1017/S0022112005005276>.
- Riquelme, A., A. Desbiens, J. Bouchard, and R. Del Villar, 2013: Parameterization of bubble size distribution in flotation columns. *IFAC Proc. Vol.*, **46**, 128–133, <https://doi.org/10.3182/20130825-4-US-2038.00073>.
- Shemer, L., and D. Liberzon, 2014: Lagrangian kinematics of steep waves up to the inception of a spilling breaker. *Phys. Fluids*, **26**, 016601, <https://doi.org/10.1063/1.4860235>.
- Sjöblom, A., and A.-S. Smedman, 2002: The turbulent kinetic energy budget in the marine atmospheric surface layer. *J. Geophys. Res.*, **107**, 3142, <https://doi.org/10.1029/2001JC001016>.
- Sreenivasan, K. R., 1995: On the universality of the Kolmogorov constant. *Phys. Fluids*, **7**, 2778–2784, <https://doi.org/10.1063/1.868656>.
- Stanley, R. H., W. J. Jenkins, D. E. Lott, and S. C. Doney, 2009: Noble gas constraints on air-sea gas exchange and bubble fluxes. *J. Geophys. Res.*, **114**, C11020, <https://doi.org/10.1029/2009JC005396>.
- Stansell, P., and C. MacFarlane, 2002: Experimental investigation of wave breaking criteria based on wave phase speeds. *J. Phys. Oceanogr.*, **32**, 1269–1283, [https://doi.org/10.1175/1520-0485\(2002\)032<1269:EOWBC>2.0.CO;2](https://doi.org/10.1175/1520-0485(2002)032<1269:EOWBC>2.0.CO;2).
- Su, M.-Y., and J. Cartmill, 1995: Effects of salinity on breaking wave generated void fraction and bubble size spectra. *Air-Water Gas Transfer: Selected papers from the Third International Symposium on Air-Water Gas Transfer*, B. Jähne and E. C. Monahan, Eds., AEON, 305–311.
- Taylor, G. I., 1938: The spectrum of turbulence. *Proc. Roy. Soc. A*, **164**, 476–490, <https://doi.org/10.1098/rspa.1938.0032>.
- Terray, E. A., M. A. Donelan, Y. C. Agrawal, W. M. Drennan, K. K. Kahma, A. J. Williams, P. A. Hwang, and S. A. Kitaigorodskii, 1996: Estimates of kinetic energy dissipation under breaking waves. *J. Phys. Oceanogr.*, **26**, 792–807, [https://doi.org/10.1175/1520-0485\(1996\)026<0792:EOKEDU>2.0.CO;2](https://doi.org/10.1175/1520-0485(1996)026<0792:EOKEDU>2.0.CO;2).
- Thorpe, S. A., 1982: On the clouds of bubbles formed by breaking wind-waves in deep water and their role in air-sea gas transfer. *Philos. Trans. Roy. Soc.*, **A304**, 155–210, <https://doi.org/10.1098/rsta.1982.0011>.
- , 1984: A model of the turbulent diffusion of bubbles below the Sea surface. *J. Phys. Oceanogr.*, **14**, 841–854, [https://doi.org/10.1175/1520-0485\(1984\)014<0841:amottd>2.0.co;2](https://doi.org/10.1175/1520-0485(1984)014<0841:amottd>2.0.co;2).
- , and A. Stubbs, 1979: Bubbles in a freshwater lake. *Nature*, **279**, 403–405, <https://doi.org/10.1038/279403a0>.
- Wang, Q., and Coauthors, 2018: CASPER: Coupled Air-Sea Processes and Electromagnetic Ducting Research. *Bull. Amer. Meteor. Soc.*, **99**, 1449–1471, <https://doi.org/10.1175/BAMS-D-16-0046.1>.
- Whalen, J., and M. Ochi, 1978: Variability of wave spectral shapes associated with hurricanes. *Offshore Technol. Conf.*, Houston, TX, Society of Petroleum Engineers, OTC 3228-MS, <https://doi.org/10.4043/3228-MS>.
- Yelland, M., and P. K. Taylor, 1996: Wind stress measurements from the open ocean. *J. Phys. Oceanogr.*, **26**, 541–558, [https://doi.org/10.1175/1520-0485\(1996\)026<0541:WSMFTO>2.0.CO;2](https://doi.org/10.1175/1520-0485(1996)026<0541:WSMFTO>2.0.CO;2).
- Young, I. R., 1997: Observations of the spectra of hurricane generated waves. *Ocean Eng.*, **25**, 261–276, [https://doi.org/10.1016/S0029-8018\(97\)00011-5](https://doi.org/10.1016/S0029-8018(97)00011-5).
- , and A. V. Babanin, 2006: Spectral distribution of energy dissipation of wind-generated waves due to dominant wave breaking. *J. Phys. Oceanogr.*, **36**, 376–394, <https://doi.org/10.1175/JPO2859.1>.